The Levitron

Master's thesis

Axel Erbing

Supervisor: Prof. Ingemar Bengtsson

Assistant supervisor: Prof. Emeritus Sven-Olof Holmgren

Assistant supervisor: Prime Engineer of Science Lars Thollander

Abstract

The Levitron® is a toy consisting of a spinning-top magnet levitating over a permanent-magnet base. This seemingly violates Earnshaw's theorem which forbids the levitation using permanent magnets with fixed orientations. This master's thesis aims to explore the theory behind the Levitron both experimentally and by numerical simulation. The working principle of the device and of a magnetic driving system used experimentally are derived along with a simple model of air resistance. Stable levitation is only possible within a certain spin-frequency interval. The spin frequency of the top is measured experimentally to determine the stable interval. The top's precession frequency is observed in relation to the driving system. The equations of motion are solved numerically and the result is analyzed and compared to the experimental measurements. The agreement between theory and experiment is satisfactory but not perfect.

Contents

1. Introduction

There are some inventions that come as a surprise to the scientific community as they seem to contradict fundamental results. One such example is the Levitron®. The Levitron is an advanced toy that consists of a small, magnetized spinning top along with a permanent magnet base. By spinning the top on a lifting plate and raising it to the appropriate height above the base, it is possible to achieve stable levitation. This is done using only permanent magnets. Successful levitation requires careful adjustments of the top mass and the alignment of the base as the range of correct parameters is very small. The top can be kept floating for several minutes until air resistance eventually slows down its spin too much causing it to fall.

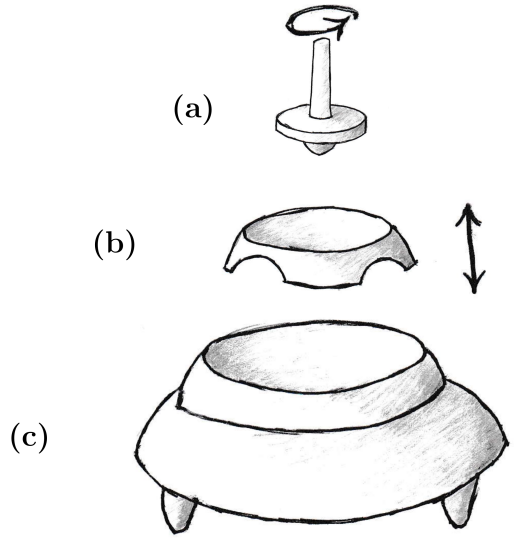

Figure 1.1: The Levitron toy with (a) top, (b) lifting plate and (c) magnetic base.

Before its discovery in 1983 by inventor Roy Harrigan, many physicists well-versed in mechanics and electrodynamics would have claimed that levitation with permanent magnets is impossible as it violates Earnshaw's theorem from 1842. The theorem is an example of a no-go theorem, a theorem which forbids a physical situation or condition. This may have discouraged many people from even trying

out similar ideas and could be the reason why something that only relies on classical physics was not discovered until the 1980s. In order for levitation to take place, the top has to be both light and strongly magnetized. The development of strong, light-weight magnets in the later half of the 20th century, and the prior lack of them, could also have held back the invention of the Levitron. Despite being told that he was wasting his time, Harrigan continued his efforts and managed to construct a top with the correct properties, to find a base magnet producing an appropriate magnetic field, and to also design a method to bring the top to the right height. Harrigan patented the device but was not able to make it commercially available.

In 1993, Roy Harrigan began collaborating with Bill Hones to commercialize the device but this endeavour did not produce any result and was soon ended. Shortly after, Hones and his father applied for a similar patent for a levitating spinning top above a square magnet base which was issued in 1995. The similarity between the two patents resulted in legal dispute which eventually ended with the company of Bill Hones winning the case and retaining all commercial rights. The details, as presented by one side of the conflict, of this can be found in ref. [9]. The patent by Hones led to the market launch of the Levitron which over time has been sold in several different models and is still available in stores today. Originally, the base was in the form of a magnetized square with a circular unmagnetized hole in the middle. Other designs such as the ring magnet, which is be used in this master's thesis, were introduced later. A driving device to counteract air resistance called the Levitron Perpetuator® has also been invented. It consists of a solenoid inside a rectangular box along with a pulse generator and switch. This provides an alternating, horizontal field to the region of levitation which keeps the top spinning at a constant rate. A modified version of the Perpetuator is used in this project.

As the apparent violation of Earnshaw's theorem suggests, the theory behind the device is rather complicated. It is not hard to figure out that the upward magnetic force on the spinning-top magnet must cancel out the downward gravitational force. The gyroscopic stability from the spin of the top prevents it from flipping but this is not enough to explain how it works. In the beginning of the next chapter, Earnshaw's theorem is stated and applied to a naive model of the Levitron to show that the problem is more sophisticated than one might think. The Levitron has been studied previously by several authors, most notably by Sir M. V. Berry who published the first article [1] on the theory of the device. Other authors include Simon et al. [10] who published a both theoretical and experimental study of the device shortly after.

The purpose of this master's thesis is to explore the theory behind the Levitron and to construct an experimental setup to measure relevant quantities such as the top's spin and precession. The validity of the theory is then tested by comparison

with the experimental result. The working mechanism behind the Perpetuator and similar driving systems are also analyzed. Finally, the Levitron system is simulated by solving the equations of motion numerically. This gives further opportunity to evaluate both the theoretical and experimental results.

The thesis is divided in these three parts. Following the introduction, a chapter devoted to the theory of the device as well as the necessary classical mechanics to describe its rotational motion. The main points of this chapter is to show under which circumstances levitation can be achieved and to derive the complete equations of motion including frictional forces and the driving system. This chapter is followed by a chapter on the experimental treatment which contains the different setups, measured results and related practical topics. The third and final part is a chapter consisting of the numerical analysis. The thesis is ended with a chapter containing conclusions and future topics that could be explored.

2. Theory

2.1 Magnetic levitation and Earnshaw's theorem

For more than one hundred years, the idea of stable, static electromagnetic levitation was thought to be impossible due to Earnshaw's theorem [3], proved by the English mathematician Samuel Earnshaw. The theorem states that it is impossible to create a stable equilibrium for a point charge using any static charge or current distribution, including permanent magnets. The same also holds for a magnetic dipole which suggests that the theorem could be applied to the Levitron.

Let us see how Earnshaw's theorem applies to a a magnetic dipole, $\boldsymbol{\mu}$, with fixed orientation and constant magnitude in a time-independent, external magnetic field, $\boldsymbol{B}$, and gravity. The potential energy, U, is given by

$$U = -\boldsymbol{\mu} \cdot \boldsymbol{B} + mgz \tag{2.1}$$

with the corresponding force

$$\boldsymbol{F}(x, y, z) = -\boldsymbol{\nabla} U = -\boldsymbol{\nabla}(\boldsymbol{\mu} \cdot \boldsymbol{B} + mgz). \tag{2.2}$$

For a stable equilibrium point, the potential energy U must have the property that its symmetric Hessian matrix H with components $H_{ij} = \partial_i \partial_j U$ is positive-definite, i.e.

$$\boldsymbol{x}^T H \boldsymbol{x} > 0, \quad \text{for all non-zero vectors } \boldsymbol{x}. \tag{2.3}$$

This in turn implies that its eigenvalues are positive and that

$$0 < \nabla^2 U = \nabla^2 \left(-\boldsymbol{\mu} \cdot \boldsymbol{B} + mgz\right) = -(\mu_x \nabla^2 B_x + \mu_y \nabla^2 B_y + \mu_z \nabla^2 B_z) \tag{2.4}$$

However by vector calculus, the magnetic field components solve the Laplace equation,

$$\nabla^2 \boldsymbol{B} = (\nabla^2 B_x, \nabla^2 B_y, \nabla^2 B_z) = \boldsymbol{\nabla}(\boldsymbol{\nabla} \cdot \boldsymbol{B}) - \boldsymbol{\nabla} \times (\boldsymbol{\nabla} \times \boldsymbol{B}) = 0,$$

where Maxwell's equations in the absence of charges, currents and electric fields,

$$\boldsymbol{\nabla} \cdot \boldsymbol{B} = 0, \quad \boldsymbol{\nabla} \times \boldsymbol{B} = 0 \tag{2.5}$$

have been used in the last equality. This implies that U also solves the Laplace equation as

$$\nabla^2 U = -(\mu_x \nabla^2 B_x + \mu_y \nabla^2 B_y + \mu_z \nabla^2 B_z) = 0 \tag{2.6}$$

which contradicts the inequality (2.4). Because of this, there cannot exist a stable equilibrium point. This system is a naive model of the Levitron where the orientation of the top is kept approximately constant due to gyroscopic stability caused by its spin. This model certainly contradicts the possibility of stable magnetic levitation and because of this, the invention of the device came as a surprise to many physicists. The theory behind it is non-trivial!

The reason why this model fails to predict stable levitation and how it can be modified to do so is discussed in the latter parts of this chapter. Before moving on to introduce the framework of rigid body mechanics, it is worth to point out that there are certain kinds of systems that display electromagnetic levitation but are not covered by Earnshaw's theorem, many of which were discovered before the Levitron was invented. For example the famous quadrupole ion trap [7] falls outside its scope as the electric fields involved do not arise from a static charge and current distribution. Magnetic levitation involving superconductors and diamagnets are also not covered by the theorem. The latter includes the famous experiment [2] where a live frog is put in stable levitation using very strong magnetic fields.

2.2 Rigid body mechanics

A rigid body can be defined in two ways. The first and simplest way is as a system of N point masses where the distance between any two is fixed in time. This object can move and rotate but will retain its shape. The second way is to consider a continuous mass distribution within some volume whose shape does not change with time. This can easily be visualized by letting the number of discrete points masses become infinite, evenly distributed inside the body. The continuous model is appropriate for describing the motion of the Levitron top. In this case, for a mass density $\rho(\boldsymbol{r})$, the total mass m is given by

$$m = \int d^3 r \rho(\boldsymbol{r}) \tag{2.7}$$

where the integral is taken over all space. Note that $\rho(\boldsymbol{r})$ is zero outside the body. When working with rigid bodies under both rotation and translation, it is convenient to introduce a body-fixed system which follows the movement of the body and a space-fixed system which remains fixed in space. The origin of the space-fixed system can be taken arbitrarily but for the body-fixed system, setting the origin to be the center of mass simplifies many important formulas. The center

of mass can be found from

$$\boldsymbol{R} = \int d^3 r \rho(\boldsymbol{r}) \boldsymbol{r}, \tag{2.8}$$

and is taken as the origin of the body-fixed system.

In order to find the energy of a rigid body, the first step is to find the velocity at any given point. For an infinitesimal translation $d\boldsymbol{R}$ of the center of mass and rotation $d\theta$ counter-clockwise around $\hat{\boldsymbol{n}}$, any point $\boldsymbol{r}$ in the body moves by [8]

$$d\boldsymbol{r} = d\boldsymbol{R} + d\phi \; \hat{\boldsymbol{n}} \times \boldsymbol{x} \tag{2.9}$$

where $\boldsymbol{x}$ is the point $\boldsymbol{r}$ in the body-fixed system. Thus, the velocity at any point is

$$\boldsymbol{v}(\boldsymbol{r}) \equiv \frac{d\boldsymbol{r}}{dt} = \frac{d\boldsymbol{R}}{dt} + \frac{d\phi}{dt} \; \hat{\boldsymbol{n}} \times \boldsymbol{x} \equiv \boldsymbol{V} + \boldsymbol{\omega} \times \boldsymbol{x} \tag{2.10}$$

where the angular velocity vector $\boldsymbol{\omega}$ has been introduced. In the continuous model, the kinetic energy of the rigid body, T, can be shown to be [8]

$$\begin{aligned} T = \frac{1}{2} \int d^3 r \rho(\boldsymbol{r}) v(\boldsymbol{r})^2 &= \frac{1}{2} \int d^3 r \rho(\boldsymbol{r}) V^2 + \frac{1}{2} \sum_{i,j} \int d^3 r \rho(\boldsymbol{r}) \omega_i \left[r^2 \delta_{ij} - x_i x_j \right] \omega_j \\ &= \frac{1}{2} m V^2 + \frac{1}{2} \boldsymbol{\omega}^{\mathrm{T}} \boldsymbol{I} \boldsymbol{\omega} \end{aligned} \tag{2.11}$$

where $r = |\boldsymbol{r}|$, δ_{ij} is the Kronecker delta and $\boldsymbol{I}$ is the inertia tensor with components

$$I_{ij} = \int d^3 r \rho(\boldsymbol{r}) \left[r^2 \delta_{ij} - x_i x_j \right]. \tag{2.12}$$

In the case of the Levitron, $\rho(\boldsymbol{r})$ is circularly symmetric and if one of the coordinate axes is chosen along the axis of symmetry, the inertia tensor becomes diagonal. Then the kinetic energy is simply

$$T = \frac{1}{2} m V^2 + \frac{1}{2} \sum_{i=1}^{3} I_i \omega_i^2 \tag{2.13}$$

which can conveniently be separated into a translational and rotation part

$$\begin{aligned} T_{\mathrm{trans}} &= \frac{1}{2} m V^2 = \frac{1}{2} m \left(\dot{x}^2 + \dot{y}^2 + \dot{z}^2 \right), \\ T_{\mathrm{rot}} &= \frac{1}{2} \sum_{i=1}^{3} I_i \omega_i^2. \end{aligned} \tag{2.14}$$

Another important quantity in rigid body mechanics is the angular momentum $\boldsymbol{L}$. It is related to the angular velocity vector by

$$\boldsymbol{L} = \boldsymbol{I} \boldsymbol{\omega} \tag{2.15}$$

where $\boldsymbol{I}$ again is taken as the matrix form of the inertia tensor. If there is no external forces on a rigid body, its angular momentum is conserved. In the presence, of external forces,

$$\dot{\boldsymbol{L}} = \boldsymbol{\tau}. \tag{2.16}$$

where $\boldsymbol{\tau}$ is the external torque.

The time evolution evolution of the angular velocity $\boldsymbol{\omega}$ obeys Euler's equations. For a diagonal inertia tensor, the equations are [8]

$$\begin{aligned} I_1\dot{\omega_1} + (I_3 - I_2)\omega_2\omega_3 &= \tau_1 \\ I_2\dot{\omega_2} + (I_1 - I_3)\omega_3\omega_1 &= \tau_2 \\ I_3\dot{\omega_3} + (I_2 - I_1)\omega_1\omega_2 &= \tau_3 \end{aligned} \tag{2.17}$$

where the right hand side are the components of $\boldsymbol{\tau}$. Note that everything in Equation 2.17 is given in the body-fixed system. These equations are very useful when the orientation of the body (and thereby its body-fixed system) is unimportant. For the Levitron, the external torque depends on both the top orientation and its position through the magnetic field of the base, making Euler's equations insufficient.

Because the angular velocity vector $\boldsymbol{\omega}$ in itself is not enough, it is clear that some new coordinates are needed to describe the rotational motion of the Levitron. The number of coordinates required is not obvious. In two dimensions, a rotation around a given point can be uniquely determined by one coordinate, normally the angle of rotation. When working in three dimensions, one needs, in order to specify a rotation, in addition to an angle a fixed axis with direction (unit vector). Any unit vector is uniquely determined by a point on the unit sphere which means that a total of three coordinates are needed. Instead of working with unit vectors, a common parametrization are the Euler angles ϕ, θ and ψ. Let x, y and z be the axes in the space-fixed system and x_0, y_0 and z_0 be the axes in the body-fixed system. The Euler angles relates to the orientation of the rigid body by three consequent rotations performed according to

1. Rotation of ϕ rad around the original z_0-axis
2. Rotation of θ rad around the intermediate x_0-axis
3. Rotation of ψ rad around the final z_0-axis.

In terms of rotation matrices

$$R_x(\theta) = \begin{pmatrix} 1 & 0 & 0 \\ 0 & \cos\theta & -\sin\theta \\ 0 & \sin\theta & \cos\theta \end{pmatrix}, \qquad R_y(\theta) = \begin{pmatrix} \cos\theta & 0 & \sin\theta \\ 0 & 1 & 0 \\ -\sin\theta & 0 & \cos\theta \end{pmatrix}, \\ R_z(\theta) = \begin{pmatrix} \cos\theta & -\sin\theta & 0 \\ \sin\theta & \cos\theta & 0 \\ 0 & 0 & 1 \end{pmatrix}, \tag{2.18}$$

the total rotation $R(t)$ can be expressed as

$$R(t) = R_{z_0}(\psi) R_{x_0}(\theta) R_z(\phi). \tag{2.19}$$

The time-dependence of ϕ, θ and ψ has been suppressed for convenience. The first rotation matrix $R_z(\phi)$ can be taken in the space-fixed system since the two systems always can be chosen to be aligned at $\phi = \theta = \psi = 0$. The rotations in the body-fixed system can be rewritten in terms of the space-fixed system by a change of coordinates. Note that after a rotation of ϕ around the z-axis, the rotation around the intermediate x_0-axis can be written as

$$R_{x_0}(\theta) = R_z(\phi) R_x(\theta) R_z^{-1}(\phi) \tag{2.20}$$

and similarly for the rotation of ψ around the final z_0-axis,

$$R_{z_0}(\psi) = \left[R_{x_0}(\theta) R_z(\phi)\right] R_z(\psi) \left[R_{x_0}(\theta) R_z(\phi)\right]^{-1}. \tag{2.21}$$

Combining this, the total rotation can be expressed using only the space-fixed system as

$$R(t) = R_z(\phi) R_x(\theta) R_z(\psi) \\ = \begin{pmatrix} \cos\phi\cos\psi - \sin\phi\cos\theta\sin\psi & -\cos\phi\sin\psi - \sin\phi\cos\theta\cos\psi & \sin\phi\sin\theta \\ \sin\phi\cos\psi + \cos\phi\cos\theta\sin\psi & -\sin\phi\sin\psi + \cos\phi\cos\theta\cos\psi & -\sin\theta\cos\phi \\ \sin\theta\sin\psi & \sin\theta\cos\psi & \cos\theta \end{pmatrix}. \tag{2.22}$$

The time derivatives of the Euler angles are often identified by the following characteristic motions of a top [4]. $\dot{\phi}$ is known as the precession which is the rotation of the body-fixed z_0-axis around the space-fixed z-axis. $\dot{\theta}$ is known as the nutation which is the nodding or swaying motion of the body-fixed z_0-axis relative to the space-fixed z-axis. ψ is known as the rotation which is the spinning of the top around the body-fixed z_0-axis. The above identification follows directly from the geometric definition of the Euler angles. The angle θ is referred to as the precession angle.

In order to write down the rotational part of the kinetic energy in terms of the Euler angles and their time-derivatives, the components of the angular velocity vector $\boldsymbol{\omega}$ are needed. The two are related by [8]

$$\omega_1 = \dot{\theta}\cos\psi + \dot{\phi}\sin\theta\sin\psi, \tag{2.23}$$

$$\omega_2 = -\dot{\theta}\sin\psi + \dot{\phi}\sin\theta\cos\psi, \tag{2.24}$$

$$\omega_3 = \dot{\phi}\cos\theta + \dot{\psi}. \tag{2.25}$$

The rotational energy can then be found from (2.14) as

$$T_{\text{rot}} = I_1(\dot{\theta}\cos\psi + \dot{\phi}\sin\theta\sin\psi)^2 + I_2(-\dot{\theta}\sin\psi + \dot{\phi}\sin\theta\cos\psi)^2 + I_3(\dot{\psi} + \dot{\phi}\cos\theta)^2. \tag{2.26}$$

For a symmetric top, i.e. $I_1 = I_2$, this expression simplifies to

$$T_{\text{rot}} = \frac{1}{2}I_1\left(\dot{\theta}^2 + \dot{\phi}^2\sin^2\theta\right) + \frac{1}{2}I_3\left(\dot{\psi} + \dot{\phi}\cos\theta\right)^2. \tag{2.27}$$

Now that coordinates for both the translational and rotational movements of a rigid body and the corresponding kinetic energy have been found, it is possible to construct the Lagrangian function L. The Lagrangian is given by the difference between the kinetic energy T and the potential energy U,

$$L = T - U. \tag{2.28}$$

From the Lagrangian, the equations of motion are found from the Euler-Lagrange equations [4],

$$\frac{d}{dt}\left(\frac{\partial L}{\partial \dot{q}_i}\right) - \frac{\partial L}{\partial q_i} = 0. \tag{2.29}$$

For a rigid body, the coordinates q_i range over the space coordinates x, y and z as well as the Euler angles ϕ, θ and ψ meaning that (2.29) are a total of six separate equations. In the next section, these equations are be written out more explicitly.

2.3 Equations of motion

Now that the mechanics governing the rotations of rigid bodies have been found, the equations of motion for the Levitron can be derived. The Levitron consists of a permanent magnet in the form of a symmetric, spinning top along with a permanent magnet base. There are different variants of the base shape and in this project a ring magnet is used. The magnetized part of the top is a small cylinder magnet and for the purpose of the theoretical analysis it will be regarded as a magnetic dipole located at the top's center of mass. Note that this involves two distinct approximations and will as a whole be referred to as the top being small. The validity of the dipole approximation is investigated later in Section 2.10.

The configuration space of the full system describing the Levitron is six-dimensional consisting of three space coordinates x, y and z determining the position of the

top and the three Euler angles ϕ, θ and ψ governing its rotation. Denoting the magnetic moment of the top dipole by $\boldsymbol{\mu}$ and the external field generated by the base ring magnet by $\boldsymbol{B}(\boldsymbol{r})$, the potential energy of the system is given by

$$U = -\boldsymbol{\mu}(\phi,\theta,\psi)\cdot\boldsymbol{B}(\boldsymbol{r}) + mgz = -\left[R(\phi,\theta,\psi)\boldsymbol{\mu}\right]\cdot\boldsymbol{B}(\boldsymbol{r}) + mgz. \tag{2.30}$$

In the last equality, the rotation matrix absorbs the angular dependence and is multiplied with the constant dipole vector $\boldsymbol{\mu}$. With the potential energy known, the Lagrangian of the system becomes

$$\begin{aligned} L =& \frac{1}{2}m\left(\dot{x}^2+\dot{y}^2+\dot{z}^2\right) + \frac{1}{2}I_1\left(\dot{\theta}^2+\dot{\phi}^2\sin^2\theta\right) + \frac{1}{2}I_3\left(\dot{\psi}+\dot{\phi}\cos\theta\right)^2 \\ &+ \left[R(\phi,\theta,\psi)\boldsymbol{\mu}\right]\cdot\boldsymbol{B}(\boldsymbol{r}) - mgz. \end{aligned} \tag{2.31}$$

Here m is the mass of the top, I_i are the moments of inertia and g is the gravitational acceleration. The equations of motion for all coordinates are obtained from the Euler-Lagrange equations and are listed below:

$$\begin{aligned} m\ddot{x} &= \left[R(\phi,\theta,\psi)\boldsymbol{\mu}\right]\partial_x\boldsymbol{B}(\boldsymbol{r}), \\ m\ddot{y} &= \left[R(\phi,\theta,\psi)\boldsymbol{\mu}\right]\partial_y\boldsymbol{B}(\boldsymbol{r}), \\ m\ddot{z} &= \left[R(\phi,\theta,\psi)\boldsymbol{\mu}\right]\partial_z\boldsymbol{B}(\boldsymbol{r}) - mg, \end{aligned} \tag{2.32}$$

$$\begin{aligned} I_1\frac{d}{dt}\left(\dot{\phi}\sin^2\theta\right) + I_3\frac{d}{dt}\left(\cos\theta\left[\dot{\psi}+\dot{\phi}\cos\theta\right]\right) &= \left[\partial_\phi R(\phi,\theta,\psi)\boldsymbol{\mu}\right]\cdot\boldsymbol{B}(\boldsymbol{r}) \\ I_1\left(\ddot{\theta}-\dot{\phi}^2\sin\theta\cos\theta\right) + I_3\sin\theta\,\dot{\phi}\left(\dot{\psi}+\dot{\phi}\cos\theta\right) &= \left[\partial_\theta R(\phi,\theta,\psi)\boldsymbol{\mu}\right]\cdot\boldsymbol{B}(\boldsymbol{r}) \\ I_3\frac{d}{dt}\left(\dot{\psi}+\dot{\phi}\cos\theta\right) &= \left[\partial_\psi R(\phi,\theta,\psi)\boldsymbol{\mu}\right]\cdot\boldsymbol{B}(\boldsymbol{r}) \end{aligned} \tag{2.33}$$

These equations are the basis of the simulation presented in Chapter 4 where the explicit form of the magnetic field is used.

2.4 Stability

It is worth to point out that the stability regarded here is not around a static equilibrium. Static stability would mean that the top is not only levitating in space but also that it has no net rotation. This kind of behavior is excluded by Earnshaw's theorem and and will therefore not be expanded on further.

Since the equations of motion are too complicated to be treated analytically, two further approximations are needed to simplify the theory. Following ref. [1], the first is that the angular momentum of the top is parallel to both its angular velocity vector as well as its symmetry axis. This approximation will be referred to as the

top being fast. Using it, the equations of motion for the spin $\boldsymbol{S}$ can be expressed as

$$\dot{\boldsymbol{S}} = \boldsymbol{\mu} \times \boldsymbol{B}(\boldsymbol{r}) = \Omega \boldsymbol{b} \times \boldsymbol{S} \tag{2.34}$$

where

$$\Omega = -\mu B/S \tag{2.35}$$

is the angular velocity of the precession, and the magnetic field has been split into a direction $\boldsymbol{b}$ and magnitude B with

$$\boldsymbol{B}(t) = B(t)\boldsymbol{b}(t). \tag{2.36}$$

The second and final assumption is that the precession is fast compared to center of mass motion of the top, i.e. $|\Omega| \gg |\dot{\boldsymbol{b}}|$. Note that the change in the direction $\boldsymbol{b}$ depends on the movement of the top. This assumption takes into account that the system has two distinct time-scales. A fast time-scale which covers the dynamics of the rotational motion and a slow time-scale which applies the translational motion. The idea is to separate these two motions into two separate systems, and is related to the quantum-mechanical Born-Oppenheimer approximation. The above approximation implies that the component of $\boldsymbol{S}$ in the $\boldsymbol{b}$-direction is an adiabatic invariant and is approximately conserved. Since the magnetic dipole vector $\boldsymbol{\mu}$ is assumed to be aligned with the spin and thereby the symmetry axis, the component

$$\mu_B \equiv \boldsymbol{\mu}(t) \cdot \boldsymbol{b}(t) \tag{2.37}$$

is also an adiabatic invariant and will be regarded as constant. The potential energy, U, of the system can using this be expressed as

$$U = mgz - \boldsymbol{\mu} \cdot \boldsymbol{B}(\boldsymbol{r}) = mgz - \mu_B B(\boldsymbol{r}) \tag{2.38}$$

where m is the top mass and g is the gravitational acceleration. Hence, the angular dependence of the potential energy has been eliminated and the problem depends only on the three spatial coordinates. This simplifies the system a great deal and for stable equilibrium points the conditions

$$\begin{cases} \nabla U = 0 & \text{(equilibrium)} \\ \partial_i^2 U > 0, \quad i = 1,2,3 & \text{(stability)} \end{cases} \tag{2.39}$$

must be fulfilled which gives restrictions to where a stable equilibrium can exist. In the next section, the magnetic field $\boldsymbol{B}$ corresponding to the ring magnet base is investigated.

Before moving on though, it is interesting to point out the similarities between Equation (2.38) and Equation (2.1) used in the naive model in Section 2.1. In that section, it was shown that due to the fact that $\boldsymbol{B}$ obeys the Laplace equation, stable Levitation is impossible. However, the magnitude $B(\boldsymbol{r})$ does not solve the Laplace equation which will be demonstrated in the next section.

2.5 Magnetic field of the base

The base magnet will be treated as a uniformly magnetized, hard ferromagnet in the shape of a ring with inner radius a, outer radius b and height h. The magnetization of a hard ferromagnet is fixed and independent of any externally applied field, in this case the magnetic field from the top. This section follows the analysis in ref. [1]. Above the base, Maxwell's equations gives $\nabla \cdot \boldsymbol{B} = 0$ and $\nabla \times \boldsymbol{B} = 0$ since no charges are present. This in turn implies that

$$\boldsymbol{B}(\boldsymbol{r}) = -\nabla\Phi(\boldsymbol{r}), \quad \nabla^2\Phi(\boldsymbol{r}) = 0. \tag{2.40}$$

where $\Phi(\boldsymbol{r})$ is the magnetic scalar potential. Taylor expanding the potential in cylindrical coordinates around $r = \sqrt{x^2 + y^2}$ for each z we get

$$\Phi(r, z) = \Phi(0, z) + \frac{1}{2}\partial_r^2\Phi(0, z)r^2 + \frac{1}{3!}\partial_r^3\Phi(0, z)r^3 + \frac{1}{4!}\partial_r^4\Phi(0, z)r^4 + ... \tag{2.41}$$

which in order to fulfil the Laplace equation becomes

$$\Phi(r, z) = \phi_0(z) - \frac{1}{4}\phi_2(z)r^2 + \frac{3}{16}\phi_4(z)r^4 + ... \tag{2.42}$$

with $\phi_n(z) = \partial_z^n\Phi(0, 0, z)$. Note that all terms odd in r vanishes since the linear term in (2.42) is zero by symmetry. The symmetry also implies the angular independence. Hence, if the magnetic potential along the z-axis is determined, the complete magnetic field can be found from (2.40). The magnitude of the magnetic field B can be computed from this and up to the second order in r it is given by

$$B(\boldsymbol{r}) = \phi_1 \text{sgn}\phi_1 \left[1 + \frac{r^2}{8}\left(\frac{\phi_2^2}{\phi_1^2} - 2\frac{\phi_3}{\phi_1}\right)\right] ... \tag{2.43}$$

Before finding the explicit form of $\phi_0(z)$, the conditions (2.39) can be now be expressed using (2.43). The conditions become

$$\begin{cases} \mu_B\phi_2 \ \text{sgn}\phi_1 > 0 & \text{(equilibrium)} \\ \mu_B\phi_3 \ \text{sgn}\phi_1 < 0 & \text{(vertical stability)} \\ \mu_B \ \text{sgn}\phi_1(2\phi_3 - \phi_2^2/\phi_1) > 0 & \text{(horizontal stability)} \end{cases} \tag{2.44}$$

which can only be fulfilled for $\mu_B < 0$ since otherwise the third inequality is always false. Inserting this, the conditions simplify further to

$$\begin{cases} (a) \quad \phi_1 \text{ and } \phi_2 \text{ have the opposite sign} & \text{(equilibrium)} \\ (b) \quad \phi_1 \text{ and } \phi_3 \text{ have the same sign} & \text{(vertical stability)} \\ (c) \quad \phi_2^2 - 2\phi_3\phi_1 > 0 & \text{(horizontal stability)} \end{cases} \tag{2.45}$$

Note that the first inequality from the equilibrium comes from the fact that the gravitational force is negative and the magnetic force on the top must counter-act it. For the actual position of the equilibrium the sum of all forces acting on the top, which can be found from the energy, must be zero. However, these calculations provide a region of potential stability which provides information without explicitly inserting values of the constants.

The magnetic scalar potential of a hard ferromagnet is [6]

$$\Phi(\boldsymbol{r}) = -\frac{\mu_0}{4\pi}\boldsymbol{\nabla}\cdot\int d^3\boldsymbol{r}'\frac{\boldsymbol{M}(\boldsymbol{r}')}{|\boldsymbol{r}-\boldsymbol{r}'|} \tag{2.46}$$

where μ_0 is the free space permeability and $\boldsymbol{M}(\boldsymbol{r})$ is the magnetization. The magnetization is defined as the dipole density of the material as a function of position. Since the base magnet is assumed to be uniformly magnetized in the z-direction, $\boldsymbol{M}(\boldsymbol{r}) = (0,0,\rho)$ with constant ρ inside the ring volume and zero outside. The above integral can be simplified by approximating the base as thin, i.e. the z' component does not contribute to the length of $\boldsymbol{r}'$ inside the volume. Hence, along the z-axis,

$$|\boldsymbol{r}-\boldsymbol{r}'| = \left(R'^2+z^2\right)^{1/2}. \tag{2.47}$$

where $R'^2 = x'^2 + y'^2$. Inserting the above into (2.46), the potential on the central axis becomes

$$\begin{aligned}\Phi(0,0,z) \equiv \phi_0(z) &= -\frac{\mu_0\rho}{4\pi}\int_A dx'dy'\left(\partial_z\int_{-h}^{0}\frac{dz'}{\left(R'^2+z^2\right)^{1/2}}\right)\\ = \frac{\mu_0\rho z}{4\pi h}\int_A dx'dy'\frac{1}{\left(R'^2+z^2\right)^{3/2}} &= z\rho\int_A dx'dy'\frac{1}{\left(R'^2+z^2\right)^{3/2}}\end{aligned} \tag{2.48}$$

where the all constants have been absorbed into ρ. Changing to polar coordinates, the final result is

$$\phi_0(z) = 2\pi\rho z\int_a^b\frac{R'dR'}{(R'^2+z^2)^{3/2}} = 2\pi\rho\left(\frac{z}{\sqrt{a^2+z^2}}-\frac{z}{\sqrt{b^2+z^2}}\right). \tag{2.49}$$

The higher order derivatives needed in (2.43) and can be computed by ordinary differentiation:

$$\begin{aligned}\phi_1(z) &= 2\pi\rho\left(\frac{a^2}{(a^2+z^2)^{3/2}}-\frac{b^2}{(b^2+z^2)^{3/2}}\right)\\ \phi_2(z) &= 2\pi\rho\left(\frac{3b^2z}{(b^2+z^2)^{5/2}}-\frac{3a^2z}{(a^2+z^2)^{5/2}}\right)\\ \phi_3(z) &= 6\pi\rho\left(\frac{a^2(4z^2-a^2)}{(a^2+z^2)^{7/2}}-\frac{b^2(4z^2-b^2)}{(b^2+z^2)^{7/2}}\right)\end{aligned} \tag{2.50}$$

2.6 Region of stability

Using the criterion (2.45), a region of potential stability can be found now that the magnetic potential along the axis is known. For the type of Levitron used, the inner and outer radius of the base are related by $b \approx 2a$. By this substitution the functions ϕ_i become

$$\begin{aligned}
\phi_1(z) &= \frac{2\pi\rho}{a}\left(\frac{1}{(1+(z/a)^2)^{3/2}} - \frac{4}{(4+(z/a)^2)^{3/2}}\right) \\
\phi_2(z) &= \frac{6\pi\rho}{a^2}\left(\frac{4z/a}{(4+(z/a)^2)^{5/2}} - \frac{z/a}{(1+(z/a)^2)^{5/2}}\right) \\
\phi_3(z) &= \frac{6\pi\rho}{a^3}\left(\frac{4(z/a)^2-1}{(1+(z/a)^2)^{7/2}} - 16\frac{(z/a)^2-1}{(4+(z/a)^2)^{7/2}}\right)
\end{aligned} \tag{2.51}$$

The functions (2.51) as well as $\phi_2^2 - 2\phi_3\phi_1$ are plotted in Figures 2.1 and 2.2. Combining the plots, two intervals that fulfil the conditions (2.45) can be identified as $0.458024 < z/a < 0.986858$ and $2.45161 < z/a < 2.65165$. The exact values are found numerically by explicitly rearranging the inequalities.

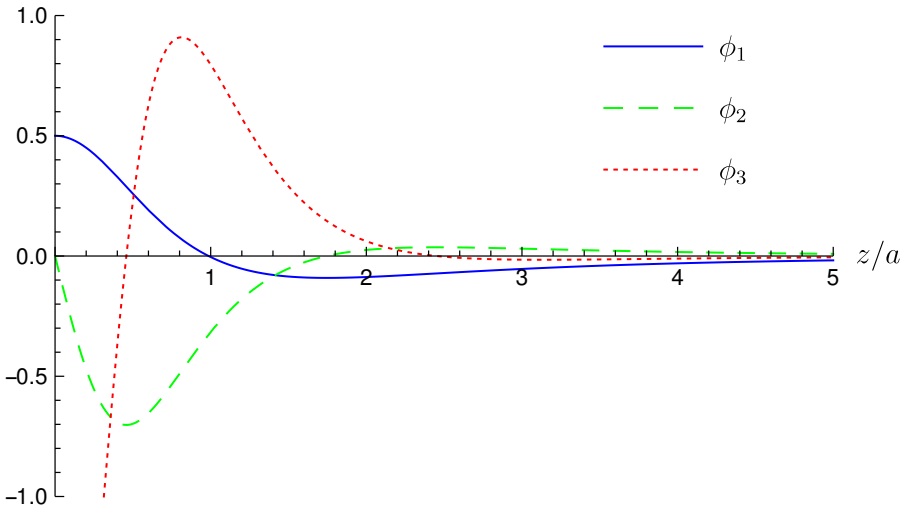

Figure 2.1: The functions ϕ_1, ϕ_2 and ϕ_3 over z/a in solid blue, long-dashed green and short-dashed red respectively.

Note that the two regions where stability is possible does not depend on the top's mass or dipole moment. As previously stated, the correct mass is critical to achieve levitation and it is interesting to find the mass range for which the equilibrium lies in the stable range. To do this, it is important to see how changes in the top's

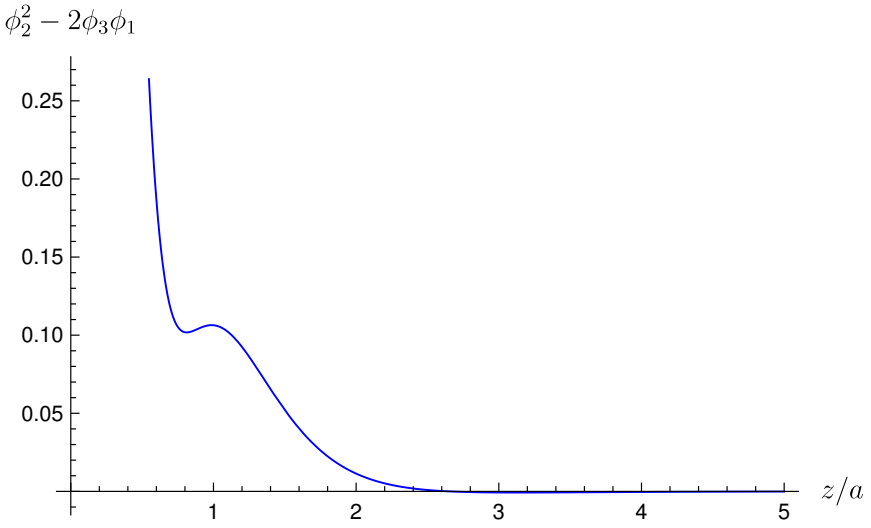

Figure 2.2: The combination $\phi_2^2 - 2\phi_3\phi_1$ over z/a. Note the sign change at approximately $z/a = 2.65$.

mass affect the energy. By rescaling the potential energy (2.38) as well as the coordinates by

$$U \to \frac{Ua}{2\pi|\mu_B|\rho}, \qquad z \to \frac{z}{a}, \qquad r \to \frac{r}{a}, \tag{2.52}$$

U can be expressed with only one parameter, the effective mass

$$M = \frac{mga^2}{2\pi|\mu_B|\rho}, \tag{2.53}$$

as

$$U(r,z) = Mz + \frac{a}{2\pi\rho}\phi_1 \mathrm{sgn}\phi_1 \left[1 + \frac{r^2}{8}\left(\frac{\phi_2^2}{\phi_1^2} - 2\frac{\phi_3}{\phi_1}\right)\right]. \tag{2.54}$$

Note that the prefactor containing a and ρ is canceled by $\phi_1(z)$ so the expression as a whole is independent of these parameters. As discussed above, $\mu_B < 0$, which is why the absolute value is used.

The upper interval corresponds to the height of levitation seen using the Levitron and will be focused on in the analysis. This does not mean that levitation in the other interval is impossible and this possibility will be investigated further below. The range of permissible top masses can be found by finding when the equilibrium lies exactly on the interval end points. This is done by solving the equation

$$F_z(0, z_0, M) = -\partial z U(0, z_0; M) = 0 \tag{2.55}$$

where F_z is the z-component of the force along the z-axis and z_0 is one of the end points. For the upper interval, $2.45161 < z/a < 2.65165$, this analysis gives the

corresponding mass range of $0.0352 < M < 0.0363$. The contours of the potential energy function U around the upper interval are shown in Figure 2.3. The plots predict the expected behavior of the top also if its mass is not chosen correctly. A too light top will fly out to the sides and a too heavy top will fall down in the center. The equilibrium can clearly be seen in subplot (b) at the expected height of $z/a \approx 2.55$.

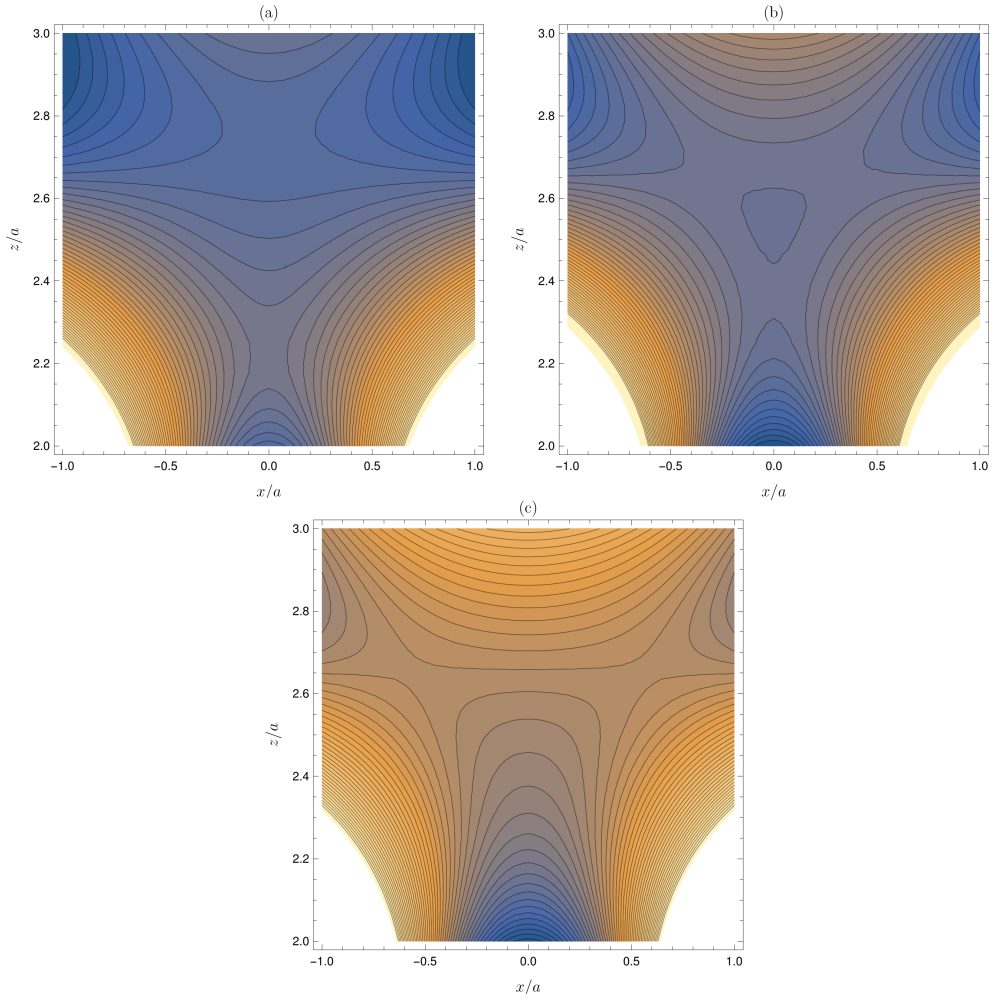

Figure 2.3: Contours of U as function of z/a and x/a. The parameter M is chosen as $M = 0.0342$ in (a), $M = 0.0360$ in (b) and $M = 0.0378$ in (c).

A similar analysis of the lower interval can be made and the potential energy also has a minimum there given that the effective mass is chosen correctly. In fact, the minimum is deeper in the lower interval, which is also larger. This suggests that it should be easier to achieve stable levitation in this interval for a wider range of masses. However, there are some problems. In this region, the magnetic field on

the axis has the opposite sign compared to that in the upper interval. This means that the top has to be spun upside down relative to its intended orientation. This causes some practical problems as the Levitron top is designed to have a relatively low center of mass which means that it can only be spun in one orientation. This can however be solved by redesigning the top and does not explain why the upper interval is chosen by the manufacturer.

Because the magnetic field is much stronger close to the base, the top cannot be spun easily below the equilibrium. As the top dipole and magnetic field are anti-parallel, it is hard to keep it in place as it will tend to flip and align itself with the field. This could potentially be solved by spinning the top above the lower interval where the magnetic field along the z-axis has the opposite sign and then lowering it into the region of stability. This would however be more complicated to implement than the simple lifting plate method. The lower interval also has the problem that the equilibrium it very close to the base which means that both the top and the lifting plate has to be very small to fit above the base. For the Levitron used in the experiment, the inner radius $a = 3.0$ cm which implies that the lower interval is located roughly 2 cm above the base.

These problems do not arise for levitation in the upper interval as the top is started close to where the z-component of the magnetic field changes sign which weakens the above effect considerably. It is also possible that the higher interval is chosen by the manufacturer simply because it is more impressive with a high levitating top.

2.7 Frequency limits

Levitation is only possible within a certain interval of angular velocities and in this section, these limits is investigated. As no such limits were found in the above analysis, in fact the spin frequency of the top is not treated directly, the loss of stability must be due to the failure of the approximations employed in Section 2.4. The lower limit is related to the fast top approximation, i.e. that the angular momentum is parallel to the angular velocity vector and the symmetry axis of the top. This condition translates into [1]

$$\omega_3 = 2\pi\nu \gg |\Omega| \tag{2.56}$$

and by substituting Ω using the relation (2.35), this becomes

$$\nu_{\min} \equiv \frac{1}{2\pi}\sqrt{\frac{mg}{I_3}\left|\frac{\phi_1}{\phi_2}\right|}. \tag{2.57}$$

The lower frequency limit is chosen as the frequency when the inequality (2.56) becomes an equality. This estimate is most likely lower than the actual limit as the approximation fails before equality is reached. Intuitively, the lower frequency limit occurs when the gyroscopic stability keeping the top upright becomes too weak causing the precession angle to become large. The vertical magnetic force acting on the top consequently becomes too small to sustain levitation. This results in the top falling down. Using the measured quantities from Chapter 3, the theoretical lower limit can be calculated to $\nu_{\min} = 14.005$ Hz.

The upper frequency limit is related to the assumption that the precession is fast, i.e. $|\Omega| \gg |\dot{\boldsymbol{b}}|$. From the relation (2.35) it is clear that Ω is decreasing as $S = I_3\omega_3$ is increasing which implies that the approximation becomes invalid for too large spin frequencies. While the lower limit ensures vertical stability, the upper frequency limit effects horizontal stability. In the limit of very large spin frequencies, the direction of the top becomes fixed and Earnshaw's theorem is applicable. This suggests that as the frequency is increased, the depth of the energy minimum in the horizontal directions is reduced and eventually the top escapes.

2.8 Magnetic driving system

The previous analysis has been for a friction-free system. Of course in reality, the Levitron cannot be levitated perpetually due to primarily air resistance. After some time, the spin of the top will become to low and it will fall down. As the top is spinning, a weak gust of air can be felt by placing the finger close to it which suggest that this has a significant effect. The slowing-down process could also potentially be caused by eddy currents in both the top and the base but this effect can be neglected since the magnetized material is ceramic and thereby not conducting.

To counteract the air resistance, a magnetic drive system consisting of an alternating horizontal field proposed in [10] is used. This field is generated from a solenoid placed under the base magnet with its length horizontally. The solenoid is fed with a sine pulse with constant (but adjustable) frequency and amplitude. Since the region of stability is rather small, the field generated will be approximated as independent of position. The generated, time-dependent magnetic field $\boldsymbol{B}_{\mathrm{d}}(t)$ is therefore taken as

$$\boldsymbol{B}_{\mathrm{d}}(t) = B_0 \sin(\omega_d t)\boldsymbol{e}_x. \tag{2.58}$$

Note that the direction is arbitrary as long as it is horizontal since the rest of the problem is completely symmetric. The mechanism behind the driving will be explored next.

In the previous sections, the magnetic moment of the top was assumed to be aligned with the symmetry axis. This is convenient for the theory but it makes the proposed driving system impossible. This can be proven easily using the Euler equations (2.17). As stated before, the form of the Euler equations makes them unsuitable for most problem with some explicit direction dependence, such as the direction of the driving field $\boldsymbol{B}_\mathrm{d}$. However in this case, an explicit solution is not required. Assume that the magnetic moment is parallel to the body-fixed z-axis, i.e. $\boldsymbol{\mu} = (0, 0, \mu)$. Then, in the body-fixed system, the Euler equations for a symmetric top for the angular velocity in the z-direction gives

$$\dot{\omega}_z = \tau_z \tag{2.59}$$

where τ_z is the z-component of the torque. The torque vector is

$$\boldsymbol{\tau} = \boldsymbol{\mu} \times \boldsymbol{B}(\boldsymbol{\omega}(t), t) \tag{2.60}$$

and hence $\tau_z = 0$ since $\boldsymbol{\mu}$ in the z-direction. Therefore, $\omega_z =$ constant for any function $\boldsymbol{B}(\boldsymbol{\omega}(t), t)$ and the spin of the top can not be accelerated (or decelerated) by a time-dependent magnetic field. Note that this result is independent of any air resistance. Since this driving system can be observed accelerating the spin of the top experimentally, the conclusion to be drawn is that that there must be a small residual component of $\boldsymbol{\mu}$ in the body-fixed xy-plane.

The driving system works by a coupling between the alternating field from the solenoid field and the above motivated horizontal component of $\boldsymbol{\mu}$.

The easiest way to visualize the working mechanism is to consider a horizontal dipole fixed in place but allowed to rotate around its center, in an horizontal magnetic field. If the dipole is aligned orthogonally to the driving field at some moment, a torque will act on the dipole to align it with the external field. If the dipole is spinning and its frequency is synchronized with the frequency of the external field, it is possible for the dipole to be accelerated continuously. This analogy is applicable as the Levitron top is kept approximately upright during levitation due to gyroscopic stability.

2.9 Model of air resistance

In order to simulate the entire system using the magnetic driving system, a frictional model of the air resistance is needed. The force related to this is often referred to as viscous torque. Because the z-component of the angular velocity is dominating, it makes sense to only implement the air resistance on this component. For a free top, this problem is straight forward using the angular velocity vector

and the Euler equations (2.17). In this case, the frictional force is just proportional to ω_3^n for some number n [5],

$$\dot{\omega}_3 = -C\omega_3^n \frac{\omega_3}{|\omega_3|} = -C\omega_3^n \operatorname{sgn}(\omega_3), \quad C > 0. \tag{2.61}$$

This formula is analogous to the viscous drag of an object in a fluid. Note that the requirement $C > 0$ as well as the sign function are needed to make sure that the friction is counter-acting the angular velocity and not the other way around. The choice of n depends on the shape of the rigid body and also the fluid it rotates in. The cases of $n = 1$ and $n = 2$ are called the Stokes' and Newton's model respectively and are the most common choices. Stokes' model is best applicable to laminar flow while Newton's model is better when the flow is turbulent. In both cases, Equation (2.61) is separable and can easily be solved. For $n = 1$, the solution is

$$\omega_3(t) = Ae^{-Ct} \tag{2.62}$$

and for $n = 2$, one obtains

$$\omega_3(t) = \frac{1}{-Ct + A} \tag{2.63}$$

where A is a constant found from the initial conditions. In the case of the Levitron top, Stokes' model with $n = 1$ is chosen and it will be justified by the experimental results in Chapter 3. Now that it is known how the frictional force from air resistance relates to the angular velocity, the next step is to translate this to the framework of Lagrangian mechanics with the Euler angles.

When dealing with friction in Lagrangian mechanics, the standard way to implement it is by adding the frictional forces directly to the equations of motion. However, it is very hard to solve for the angular velocity ω_3 in the first equation in (2.33) so it is not obvious how this frictional torque in (2.61) should be added. One way to add frictional forces in general is using the Rayleigh dissipation function, $\mathcal{F}$, for $n = 1$ defined as [4]

$$\mathcal{F} = \frac{1}{2} \sum_{i=1}^{N} D_{ij} \dot{q}_i \dot{q}_j \tag{2.64}$$

together with modified Euler-Lagrange equations

$$\frac{d}{dt}\left(\frac{\partial L}{\partial \dot{q}_i}\right) - \frac{\partial L}{\partial q_i} + \frac{\partial \mathcal{F}}{\partial \dot{q}_i} = 0. \tag{2.65}$$

Note that the coefficient matrix D_{ij} may depend on the position coordinates, in this case ϕ, θ and ψ. The Euler-Lagrange equation for ψ for a free top, (2.33) with $\boldsymbol{B} = 0$, with the added Rayleigh dissipation function $\mathcal{F} = C\left(\dot{\psi} + \dot{\phi}\cos\theta\right)^2/2$ is

$$I_3 \frac{d}{dt}\left(\dot{\psi} + \dot{\phi}\cos\theta\right) + C\left(\dot{\psi} + \dot{\phi}\cos\theta\right) = 0. \tag{2.66}$$

Using the relation between ω_3 and the Euler angles (2.25), this equation is identical to (2.61). Hence, it is clear that the the proposed $\mathcal{F}$ is the minimal function producing the wanted air resistance since any other of friction is neglected. Now, the equations of motion can be updated to incorporate the air resistance,

$$\begin{aligned} I_1 \frac{d}{dt}\left(\dot{\phi}\sin^2\theta\right) + I_3 \frac{d}{dt}\left(\cos\theta\left[\dot{\psi}+\dot{\phi}\cos\theta\right]\right) \\ = \left[\partial_\phi R(\phi,\theta,\psi)\boldsymbol{\mu}\right]\cdot\boldsymbol{B}(\boldsymbol{r}) - \frac{C}{I_3}\cos\theta\left(\dot{\psi}+\dot{\phi}\cos\theta\right) \\ I_1\left(\ddot{\theta} - I_1\dot{\phi}^2\sin\theta\cos\theta\right) + I_3\sin\theta\ \dot{\phi}\left(\dot{\psi}+\dot{\phi}\cos\theta\right) = \left[\partial_\theta R(\phi,\theta,\psi)\boldsymbol{\mu}\right]\cdot\boldsymbol{B}(\boldsymbol{r}) \\ I_3\frac{d}{dt}\left(\dot{\psi}+\dot{\phi}\cos\theta\right) = \left[\partial_\psi R(\phi,\theta,\psi)\boldsymbol{\mu}\right]\cdot\boldsymbol{B}(\boldsymbol{r}) - \frac{C}{I_3}\left(\dot{\psi}+\dot{\phi}\cos\theta\right). \end{aligned} \tag{2.67}$$

2.10 Validity of the dipole approximation

The fact that the magnetized part of the top is regarded as a dipole may seem hard to justify considering how large the magnetized part of the top is compared to the top as a whole, see Figure 1.1. To investigate the validity of the approximation, the energies of a dipole and a magnetized disc is compared. For this purpose the top is assumed to be uniformly magnetized along the z-direction. The energy of a uniformly magnetized volume in an external magnetic field is

$$U = -\int_V \boldsymbol{M}\cdot\boldsymbol{B}(\boldsymbol{r})d^3\boldsymbol{r} \tag{2.68}$$

where $\boldsymbol{M}$ is the magnetization or dipole density. As a reminder, the energy of a dipole in an external field is

$$U = -\boldsymbol{\mu}\cdot\boldsymbol{B}(\boldsymbol{r}) \tag{2.69}$$

and if $\boldsymbol{B}$ is assumed to be constant inside the top, the energy the two equations become equivalent. Therefore, the underlying assumption is that the magnetic field $\boldsymbol{B}(\boldsymbol{r})$ varies only little over small volumes comparable to the size of the magnetized part of the top.

The relevant quantities such as the size of the top are determined in Chapter 3 and are used here to evaluate the approximation. The magnetization of the top $\boldsymbol{M}$ is computed from the height of the equilibrium given the explicit form of $\boldsymbol{B}(\boldsymbol{r})$. Note that the above energy equations depends on both the position and the orientation of the top and for simplicity, only the z-axis, close to the equilibrium is considered. Because of this, only the angle θ has to be treated due to the circular symmetry. Numerical calculations shows that the difference in energy is less than 1 % for 6.5 cm $< z <$ 8 cm and $0 \leq \theta \leq \pi/2$. The small difference justifies the approximation which considerably simplifies the problem.

3. Experiment

3.1 The Levitron

In this chapter, the different experimental setups and components used will be discussed. Before going in to details about the more advanced setups, it is important to explain how the Levitron toy is used by itself.

As mentioned earlier, the mass range that permits levitation is quite narrow and is dependent of magnetic field strength of the base as well as the dipole moment of the top. This becomes a problem since the magnetization varies with temperature. Higher temperature weakens the field strengths which requires a lighter top and vice versa. A temperature change less than 1° C can be enough to make a previously levitating top too light or too heavy. The solution to this problem by the manufacturer is two provide a set of washers with the device that can be attached to the top using an O-ring. See Figure 3.1 below.

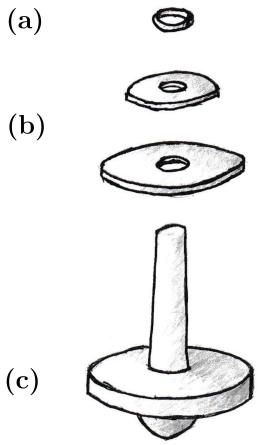

Figure 3.1: The Levitron top and washers where (a) O-ring, (b) washers and (c) top. The magnetized part of the top is the disc-like cylinder in (c).

For the Levitron used in this project, the mass of the washers ranges from the heaviest at 3.4 g to the lightest at ~ 0.1 g. Because of the temperature sensitivity, the top's mass often has to be adjusted, sometimes several times per session.

Levitation also requires the base to be highly horizontal. A slightly tilted base will result in the top falling off to one side. The correct alignment is achieved by raising or lowering the leg by turning them.

To start the device, the top is spun on the lifting plate which is then elevated a few centimeters above the base. If the top has the correct mass, it should gently lift from the lifting plate by itself just below the equilibrium. It may be spun by hand but this is rather tricky and requires a combination of skill and luck. For a more consistent result, a clever device called the Levitron Self Starter may be used. It is a small battery-driven rod that is attached to the upper part of top, spinning it up to the appropriate angular velocity while keeping it in place. The Self Starter is included in some editions of the Levitron but may also be purchased separately. A typical run lasts approximately 2 minutes.

To perform the numerical analysis of the equations of motion, (2.32) and (2.33), and compare the results to the experiments, several quantities are needed. Some measurements are therefore necessary. For the top, its mass m, moments of inertia I_i and its magnetic dipole moment $\boldsymbol{\mu}$ are needed. For the base, the inner radius a and outer radius b as well as the dipole density ρ related to its magnetic field are required. All masses are measured using a simple scale and any dimensions are found using a calliper. To compute the moment of inertia using (2.12), the washers, magnetized disc and the plastic stem are assumed to be cylindrical with uniform mass distribution. The strength of the magnetic field from the base along the z-axis is found using a Hall-plate magnetometer. This gives ρ as it is the only parameter besides a and b. The magnetic moment is harder to measure as the magnetic field of a magnetized disc differs from an ideal dipole, especially very close to the disc. Instead, the location of the equilibrium is measured and the magnetic moment is found from the force equation

$$F_z = mg - \mu \partial_z B_z(0, 0, z). \tag{3.1}$$

For the simulation, it is not important for the measured quantities to be of the utmost accuracy since the goal is to analyze the general behavior. This motivates the rather imprecise method to determine the moment of inertia and the dipole moment. Also, the frequency limits are not critically dependent on any of these two quantities making them less important. The results are presented in the table below. Note that $I_1 = I_2$ as the top is symmetric. The equilibrium height is measured to 7.3 cm and the cylindrical magnetized part of the top is measured to have a radius of 1.44 cm and height of 0.33 cm.

a (cm)	b (cm)	ρ (g cm^{-1} mT^{-1})	I_1 (g cm^2)	I_3 (g cm^2)	μ (g cm^2 mT^{-1})	m (g)
3.0	5.5	140.0	10.4	17.3	$7.14 \cdot 10^3$	25.5

Table 3.1: Table of measured quantities of the Levitron top and Base.

3.2 Driving system

When every important property of the toy itself is known, it is time to move on to the magnetic driving system. The Levitron Perpetuator as mentioned in the introduction consists of a horizontal solenoid, pulse generator and switch, placed inside a plastic, rectangular box large enough for the magnetic base to fit on top of it. When turned on, the pulse generator and switch feeds a fixed-frequency, positive square signal into the solenoid which produces an alternating, approximately horizontal magnetic field which is used to counteract air resistance.

For the average toy user, this setup is simple to use and enough to trap the top in perpetual levitation. However, there are some problems that make it unsuitable for experiments. The fixed-frequency means that the angular velocity of the top will not change notably and therefore the two frequency limits cannot be tested. The fact that the square signal has constant sign means that the driving system cannot be turned off in the middle of a session. Doing so would result in the top falling off to the side. The reason for this is that the horizontal field is not truly alternating but oscillates between zero and some value, with the corresponding field always pointing with the same direction. This have to be corrected by adjusting the alignment of the base but this means that it will not be properly aligned if the Perpetuator is turned off.

The square pulses by themselves are also a problem since their mathematical treatment is much more complicated than for example a trigonometric function. Because of this, the pulse generator and switch of the Perpetuator are replaced with an external, amplified pulse generator with adjustable frequency and amplitude which permits both signs. The shape of the signal can be chosen from sine, triangular or square waves. With this modified driving system, all the above problems are solved and many of the interesting properties can be investigated.

In order for the driving system to work, the top spin frequency must be synchronized with the driving. This is accomplished by spinning up the top to a frequency faster than the driving frequency and letting it slow down to the correct one by the air resistance. It is quite hard to achieve perpetual levitation and far from all attempts are successful. The most fruitful method is found to be leaving the top on the lifting plate until synchronization, which is shown by a prominent circular precession and constant angular velocity, and then lifting it to the appropriate

height.

3.3 Spin frequency counter

In this section, a setup to observe the spin of the top is described. The spin, or more precisely the z-component of the angular velocity vector ω_3, is important when investigating the upper and lower stability limits and other relations. This setup is similar to the one presented in ref. [10].

The idea is to use reflected light pulses to measure the spin. To do this, a piece of white tape is attached to the upper washer of the top and a strong DC lamp is set up above the base. A convex lens is placed at an angle so that light emitted from a levitating top is focused into a phototransistor. The phototransistor is connected to a frequency counter and an oscilloscope. The setup is visualized in Figure 3.2.

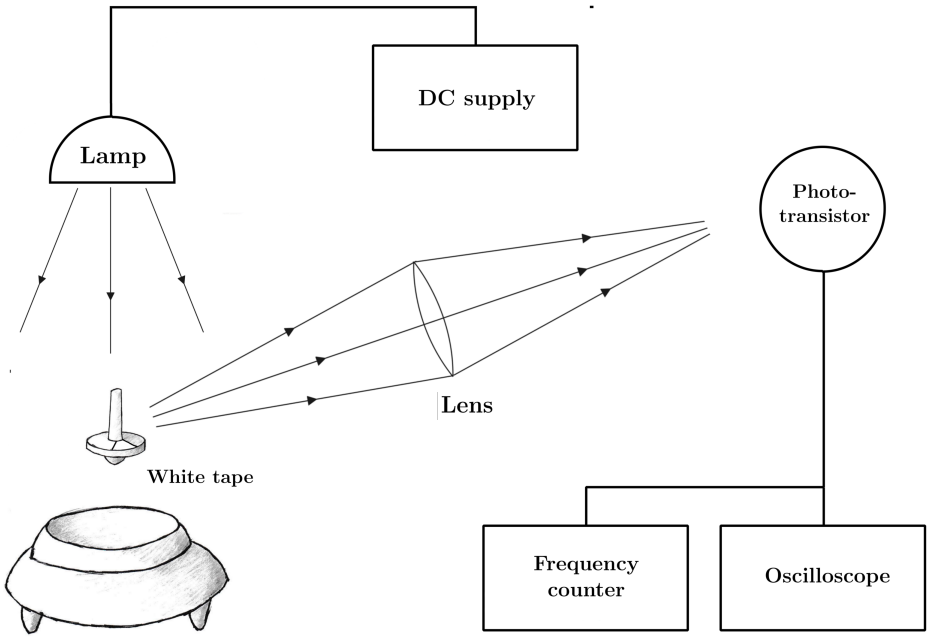

Figure 3.2: A schematic diagram over the setup to measure the top spin frequency.

Once per revolution, the light from the overhead source is reflected into the phototransistor. This gives rise to a periodic signal, whose frequency is measured by either the frequency counter or the oscilloscope. The measured quantity is the

z-component of the angular velocity ω_3, in terms of its frequency ν_3. The two quantities are related by

$$\omega_3 = 2\pi\nu_3. \tag{3.2}$$

This setup is straightforward but there are some important properties required for it to work. The material of the reflective material attached to the top has to be dull, i.e. it reflects diffuse light. The convex lens must also be placed so that the levitating top is slightly closer than the focal length. Together, these two conditions ensures that the transistor will receive the light pulses, even as the top bobs around the equilibrium.

When trying out this setup, it was discovered that the washers were not rotating with the rest of the top but instead slides on the magnetized part and on each other. This reduces the measured frequency and leads to unexpected results, especially the relation between the frequency of the driving field ν_d and the spin frequency of the top. As concluded in Section 2.8, these two quantities should be equal when equilibrium has been reached. To further add to the confusion, the results of the attempt to measure the lower frequency was very close to the results of the numerical analysis presented in Chapter 4 and also agreed with the theoretical prediction in Section 2.7. This agreement delayed the discovery of the gliding significantly and other causes were investigated instead. To prevent this phenomenon, the washers were attached to top using glue. The behavior of the top is changed significantly by this and the details as well as a possible explanation is given in Section 3.6 below.

This setup is primarily used to determine the upper and lower stability limits of the top. For the lower frequency limit, the top is spun and trapped at some frequency using the driving system. When the translational motion has stabilized after a few minutes, the driving field is turned off and the top is allowed to slow down until it falls down. The minimum frequency recorded and the results of these attempts are presented in Table 3.2. To measure the upper frequency limit, the top is as before kept at a constant frequency using the driving system and allowed to stabilize. By very slowly changing the driving frequency ω_d, the frequency of the top changes with it. Using this technique, the top is accelerated until it flies off the base and the maximum frequency is noted. The measured lower

Measurement	1	2	3	4	5	6	7	8	9	10
ν_3 (Hz)	21.7	21.4	21.7	21.9	21.8	22.3	21.8	22.0	22.1	21.9

Table 3.2: Table of measured lower frequency limits.

frequency limits have a mean value of 21.86 Hz. All measured values are higher than the theoretical estimation of approximately 14 Hz. The results of upper frequency-limit measurements are inconclusive. For high spin frequencies, the

driving synchronization breaks down and the starts to slow down. There is no reason for this to occur at the upper frequency limit which suggests that the limit has not been reached. The largest observed synchronized spin frequency is approximately 61 Hz, which at least provides a lower bound for the limit.

3.4 Precession frequency counter

An interesting relation in the Levitron system is the relation between the spin of the top and its precession angular velocity Ω. Note that for a free top, the spin (and thereby the angular velocity) is related to Ω by Equation (2.35). It is not clear if this relation is preserved for a driven top and initial experimental observations suggests that this is not the case. To investigate this, a helium-neon laser is mounted on an adjustable platform at some distance from the base such that the beam passes through the equilibrium point. The platform is calibrated so that the beam passes precisely next to the upper stem of the top. A phototransistor is placed on the other side of the top, connecting to the beam from the laser. This setup is shown in Figure 3.3.

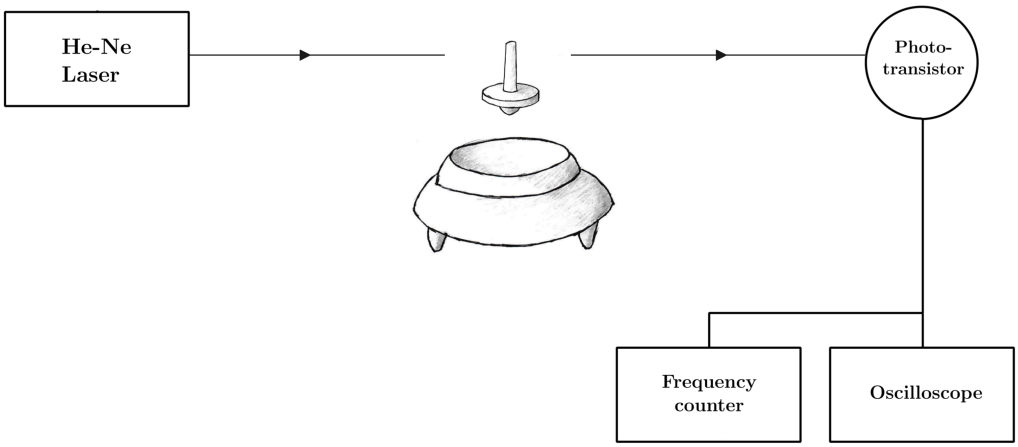

Figure 3.3: A schematic diagram over the setup to measure the top precession frequency.

When the top is somewhat stable in space, its precession periodically blocks the beam which allows its frequency to be measured using the phototransistor connected to the frequency counter and oscilloscope. The result is presented in Figure 3.4. The relation between the precession and the driving frequency, and thereby the spin frequency, is linear which is very different form the inverse-proportionality relationship of the undriven top. Note that the precession frequency is very close to the driving frequency in all points and the two quantities can be considered to

be equal or synchronized.

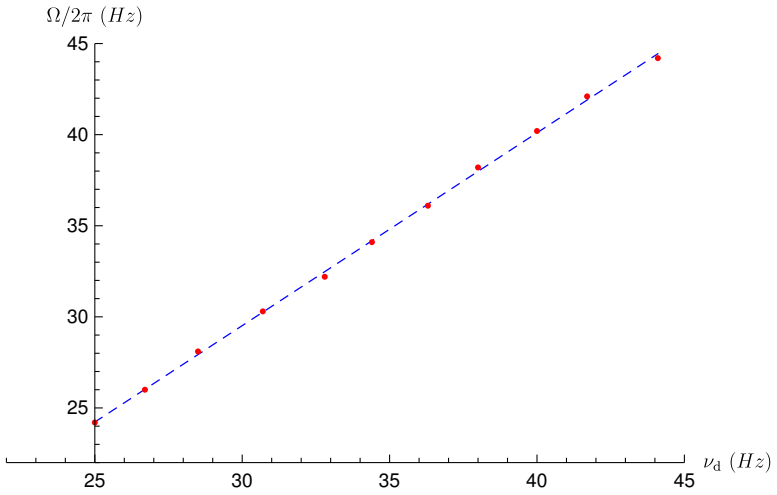

Figure 3.4: Measured top precession frequency $\Omega/2\pi$ as a function of the driving frequency ν_d in red. The dashed blue line is the least square linear fit with a slope of 1.05.

3.5 Air resistance

In this section, the setup to determine the frictional force from air resistance responsible for slowing down the spin of the top is described. As stated in Chapter 2, the choice of model to describe this force is between Stokes' model and Newton's model, Equation (2.61) with $n = 1$ and $n = 2$ respectively. Both models are fit to the measured data to determine which is more appropriate which justifies the choice for the numerical analysis in Chapter 4.

For each attempt, the top is accelerated to a frequency of 40 Hz using the driving system. The driving system is subsequently turned off and the top is allowed to slow down until it reaches the lower spin limit. Using the frequency counter, the angular velocity is measured in ten second interval. Both models can be linearized, by logarithmation in the case of Stokes' model and inversion in the case of Newton's model. Because of this, a straightforward linear least square fit is used to determine the proportionality parameter C as well as the constant given by initial condition. A total of four attempts are performed and the results are shown in Figure 3.5. From the four plots it is clear that neither of the models seem to be a perfect fit but both are quite close to the experimental data. Because of this, the Stokes' model is chosen to be implemented in the simulational analysis as the extra terms in Equation (2.67) are less complicated. The mean of the four

values, $\bar{C}_1 = 0.00318175$, for the preferred model is taken for the simulation in Chapter 4.

3.6 The effects of loose washers

It is interesting to consider how the sliding of the washers affect the general behavior of the Levitron. When the washers are loose, only held in place by the o-ring, the top is easier to start and synchronize with the driving system. The translational movement becomes smaller and after some time the top becomes almost fixed in place. It is also easier to accelerate the top by changing the driving frequency and the range of frequencies that can be attained is greater, reaching up to 66 Hz, if taking the driving frequency as the true spin frequency. A very simple model that take at least part of this effect into account is to add a spin dependence to the moment of inertia, i.e. $I_3 = I_3(\omega_3)$. This means that as the top is spinning faster, its moment of inertia becomes weaker as an effect of the washers not rotating as fast. In order for the model to be implemented into the equations of motion, the exact dependence must be known which makes this seemingly simple addition rather complicated. Because of this, the effect is not explored further. The washers are also not only sliding but also wobbling around slightly. It is possible that this movement affects the stability but this kind of behavior is even more complex.

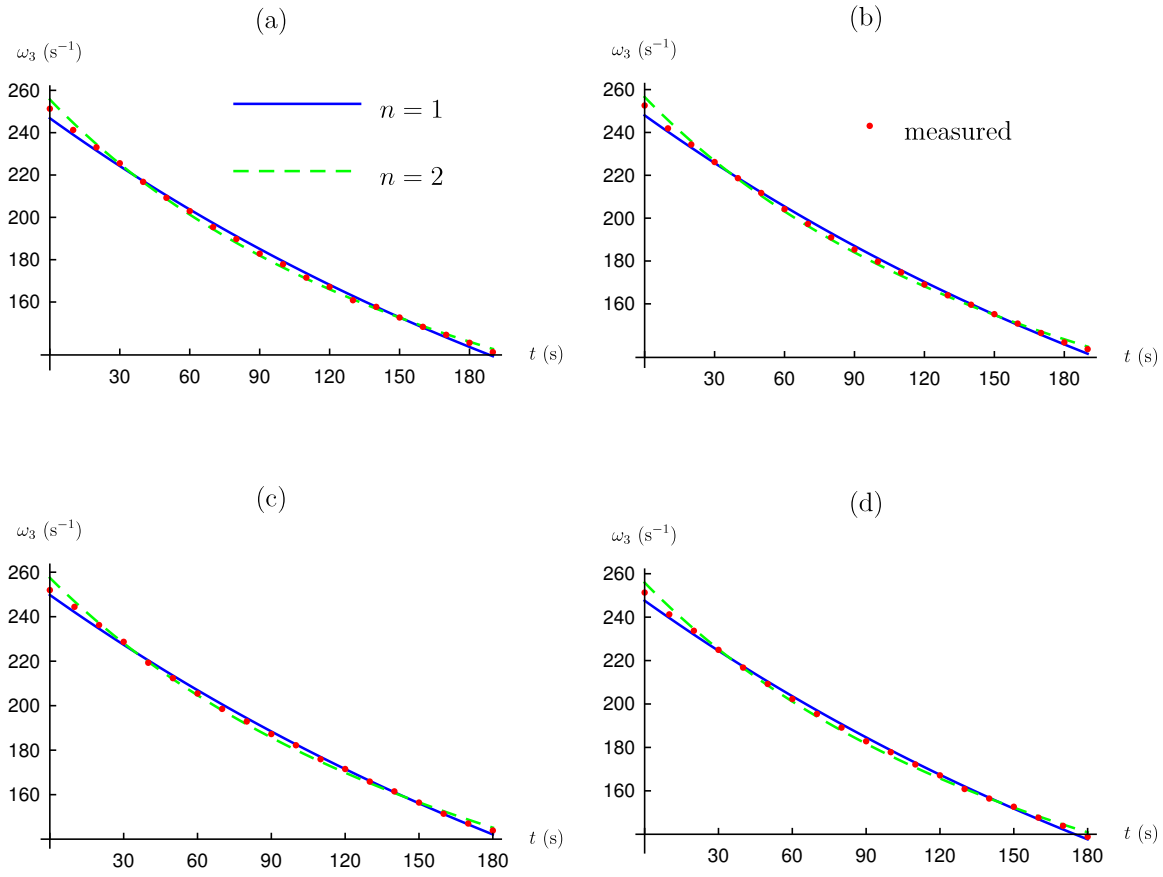

Figure 3.5: The measured z-component of the angular velocity, ω_3 as function of time for a non-driven top along with fitted models. The calculated proportionality constants are $C_1 = 0.003199$ and $C_2 = -0.00001760$ for (a), $C_1 = 0.003134$ and $C_2 = -0.00001707$ for (b), $C_1 = 0.003133$ and $C_2 = -0.00001669$ for (c) and $C_1 = 0.003261$ and $C_2 = -0.00001772$ for (d)

4. Simulation

In this chapter, the equations of motion (2.33) are solved numerically and from the results, many of the properties previously discussed are investigated. As a reminder, the equations of motion only rely on the assumption that the top is small, i.e. that is can be approximated as a dipole located at the center of mass. Because of this, the validity of the other approximations can be also studied.

The equations of motion are solved using Mathematica 10 with the built-in NDSolve-function which solves ordinary differential equations numerically. With the default settings, the function analyzes the equations and chooses a suitable method. However, for clarity, the Backward differentiation formula method is chosen for all computations in this section. The Backwards differentiation formula is an example of a linear multistep method which computes the next solution point using the information of up to six previous steps. More detailed information about this method is available in ref. [11]. A sample of the source code used in this chapter is available in Appendix A.

4.1 Initial conditions

In order to perform a simulation, the initial condition of the system must be completely specified. This includes all six coordinates and their first derivatives giving a total of twelve values that must be chosen. The only restriction given is that the coordinate θ must be non-zero to avoid division by zero during some step of the method. Different initial conditions are necessary to make sure that the simulated properties such as the lower stability limit are truly intrinsic. A total of four initial conditions are chosen for the analysis in the first part of this chapter and are shown in Table 4.1 below.

The first initial condition is chosen to be close to the experimental setup. The top is initially slightly below the equilibrium close to the z-axis moving upwards which corresponds to the top being lifted up using the lifting plate. The second initial condition corresponds to a top very close to the equilibrium point and the third represents a top far away both horizontally and vertically. In the fourth initial condition, the values from the first initial condition is reused but with an increased precession angle θ. In every case, derivatives of the first and third Euler

Initial condition	1	2	3	4
x	0.10	0.01	0.50	0.10
z	7.10	7.30	7.25	7.10
$\dot{x}$	-0.07	0.00	-0.20	-0.07
$\dot{z}$	0.20	0.00	0.05	0.20
θ	0.01	0.01	0.01	0.10
$\dot{\theta}$	0.00	0.00	0.00	0.00

Table 4.1: Table of initial conditions used in the simulation. The units are in cm, cm s^{-1} and s^{-1} where appropriate.

angle, $\dot{\phi}$ and $\dot{\psi}$, are chosen to be equal and such that

$$\omega_3 = \left(\dot{\phi}\cos\theta + \dot{\psi}\right) = 2\pi\nu_3 \tag{4.1}$$

where ν_3 is the initial spin frequency. Hence,

$$\dot{\phi} = \dot{\psi} = \frac{2\pi\nu_3}{1+\cos\theta}. \tag{4.2}$$

The time-derivative of the precession angle, $\dot{\theta}$, is initially chosen as zero. The initial values of ϕ and ψ are not important, even if the misalignment of the top's dipole and symmetry axis is implemented for the driven top. In all cases, both ϕ and ψ are initially set to zero.

4.2 Undriven top without friction

The first and simplest case that is implemented in the simulation is the friction-free, undriven Levitron. This case serves as a way to check that the method produces reasonable results before any more complicated terms are added to the equations of motion. This is also the system closest to the pure theoretical analysis. In Figure 4.1, the trajectory of the top projected on the xz-plane is shown for the four initial conditions. The plots suggests that the simulation is working as intended as the top is trapped close at the predicted height. As a reminder, in Section 2.6 the location of the equilibrium was predicted to be in the interval $2.45 < z/a < 2.65$ which with the experimental value of the inner radius $a = 3.0$ cm becomes $7.35 < z < 7.95$. The amplitude of the translational oscillations are similar in size to those that can be observed experimentally.

Note that the location of the stable equilibrium is just outside the predicted interval. This is likely due to the fact that when deriving the interval, the relation between the inner and outer radius were assumed to be $2a = b$, which is not the

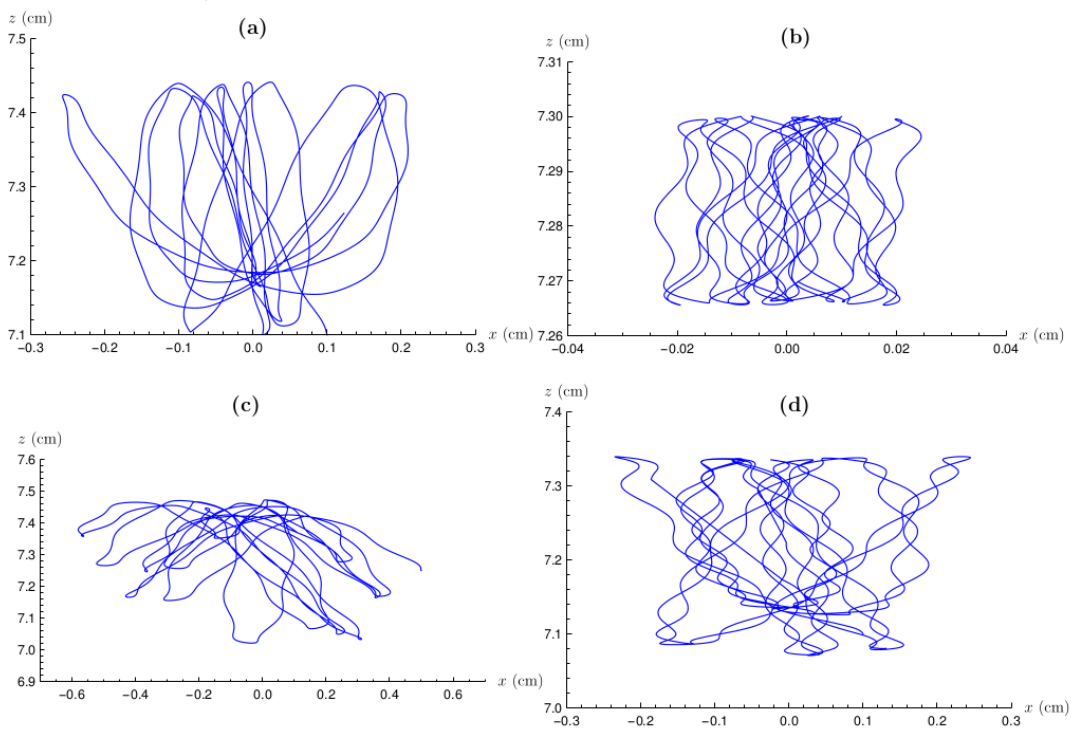

Figure 4.1: The top's position projected in the xz-plane. (a) corresponds to the first initial condition, (b) to the second and so forth. All simulations are runs are carried out over 10 seconds.

experimentally measured relation of $11/6a = b$ used in the simulation. This difference is likely to slightly alter the location of the minimum. Note that in the subplot (d), the equilibrium position seems to be located lower than in the other plots. This is because that the initial precession angle θ is larger meaning that the average horizontal magnetic force is lower.

By running the simulation with different initial spin frequency ν_3, both the lower and upper stability limits can be found. If the top escapes the equilibrium within 30 seconds, it is considered to be unstable and stable otherwise. Here, an escape from the equilibrium is taken to be when

$$\sqrt{x^2 + y^2} > 2 \text{ cm} \quad \text{or} \quad z \leq 0 \text{ cm} \tag{4.3}$$

which means that either the top has fallen to the ground or has flown away radially. In Table 4.2, the upper and lower limits are presented for a four different initial conditions. As seen in the table, the stability limits varies slightly with the initial conditions. The increased precession angle seems to be the most important factor. The time limit of just 30 seconds may affect the result, especially the second

simulation. Because the top is initially stationary and very near the equilibrium in that case, it is likely that it takes longer for an unstable top to escape. The calculated lower limits are slightly higher than the experimental results which is to be expected. This is because if the top is unstable and falls down within 30 seconds without friction, it will have some additional time to slow down further shifting the final values down.

Simulation	1	2	3	4
ν_{lower} (Hz)	22.06	21.78	22.27	23.02
ν_{upper} (Hz)	70.90	81.73	70.50	65.01

Table 4.2: Table of the simulated lower and upper limits for an undriven top without friction.

The behaviour of the top just outside the limits are shown in Figure 4.2 below. As expected with spin frequencies below the lower limit, the top eventually falls down. As mentioned before, the precession angle becomes increasingly larger until the upward magnetic force on the top becomes weaker than the gravitational force. This can be seen in Figure 4.3 which corresponds to the left plot in Figure 4.2.

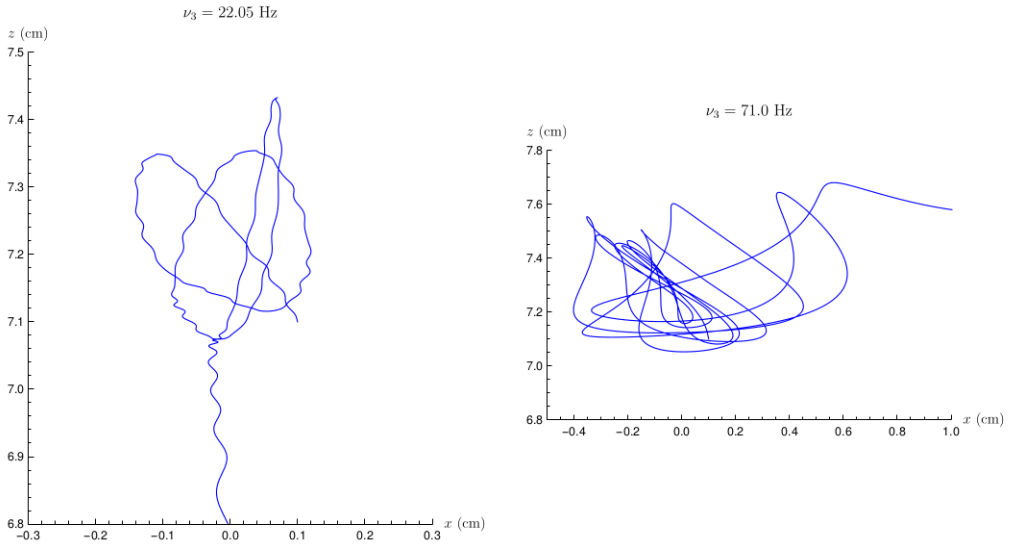

Figure 4.2: The top's position projected in the xz-plane for a too slow and too fast top respectively. In both plots, the first initial condition is used.

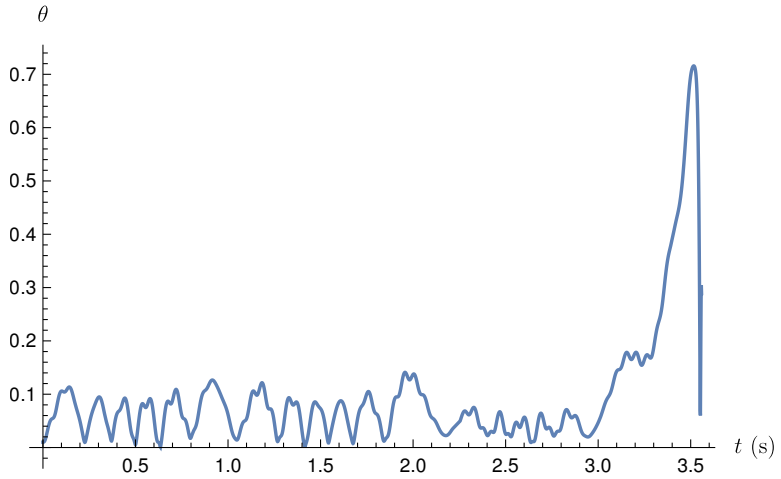

Figure 4.3: The precession angle θ as a function of time for a top just below the lower frequency limit. Note that θ becomes very large at approximately 3.4 s which forces the top out of the stable region.

4.3 Undriven top with friction

By adding the frictional forces in the equation of motion (2.67), the undriven top analogous to what is observed in the lab can be studied. This system is not suitable to find the upper stability limit but the experiment to measure the lower stability limit in Chapter 3 can be simulated. This is done by given the top an initial spin frequency of 30 Hz and simulating it until it reaches a height of $z = 6$ cm. The top will continue slowing down during its descent and if the spin frequency at $z = 0$ would be taken a lower limit slightly lower than the corresponding experimental measurement would be obtained. The final spin frequency of is recorded and presented in Table 4.3 below. The results are very close to the experimental measurements, better than the friction-free case. As before, the initial condition with the slightly larger initial angle θ has the most notable effect on the limit.

Simulation	1	2	3	4
ν_{lower} (Hz)	21.86	21.65	21.81	22.90

Table 4.3: Table of the simulated lower stability limits for an undriven top with friction.

As observed by ref. [10], if the magnetic moment is not purely axial, the top should fall down sooner. This feature can be tested numerically with the included frictional forces. Using the same initial conditions, the Levitron is simulated with and without a small misalignment of the magnetic moment. The misalignment is taken as approximately 1.5 degree towards the body-fixed x-axis, i.e.

$$\boldsymbol{\mu} = (0.03, 0, 0.97)\,\mu. \tag{4.4}$$

In both cases, the top is started with a spin frequency of 30 Hz and simulated until it falls down. By changing the direction of the magnetic moment while using the same precession angle for the two runs, the magnetic force on the top will be weaker. This implies that the mass of the top must be slightly lowered in the tilted dipole case. With exception of the mass, all parameters are equal for the two simulations. The z-components of the two simulations as well as the spin frequencies are plotted in Figure 4.4 and 4.5.

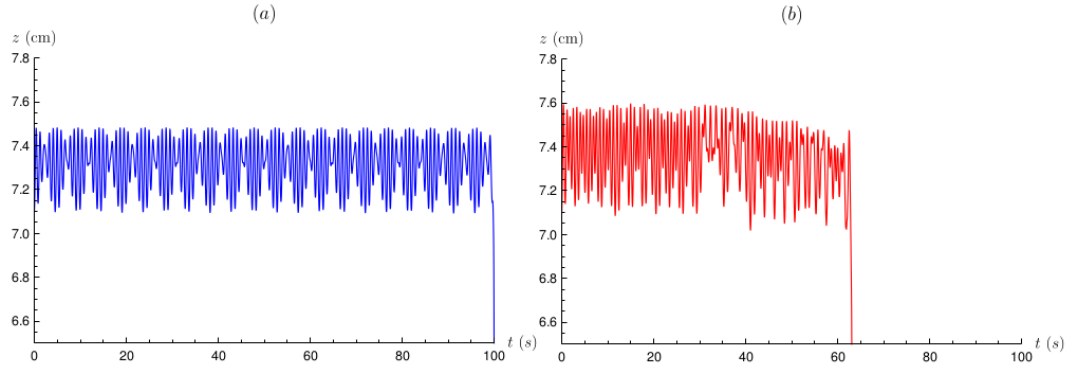

Figure 4.4: The height of the top as a function of time with (b) and without (a) misalignment between dipole moment and symmetry axis. The simulation is computed using the first initial condition.

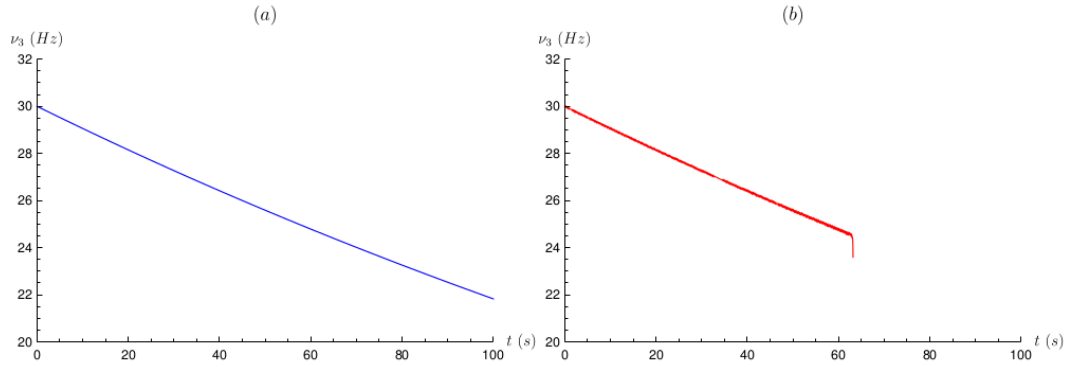

Figure 4.5: The spin frequency of the top as a function of time with (b) and without (a) misalignment between dipole moment and symmetry axis. The same simulation is used as in Figure 4.4.

As evident from the plots, the runtime is decreased but this is not caused by the top slowing down faster but rather that the lower stability limit is higher. The intuitive reason why this occurs is that for the same precession angle, the misalignment causes the vertical force to be stronger or weaker depending on the angles ϕ and ψ. This increases the amplitude of the vertical oscillatory motion, see Figure 4.4, and hence reduces the stability. The transversal component of the

dipole moment gives rise to some torque along the body-fixed z-axis but this effect is negligible compared to the air resistance. However, it is visible in the plot as a slight smearing of the curve.

The misalignment between the dipole moment and symmetry axis, which is required to magnetically control the spin frequency, decreases the runtime by approximately 35 % for an average initial spin frequency. This is quite significant and means that a drivable top is less suitable for an undriven setup.

4.4 Driven top with friction

The final and most complete system that is simulated includes both the frictional forces from air resistance and the magnetic field from the driving system. The equations of motion used are the same as in the previous section but with the additional driving component of the magnetic field from Equation (2.58). In Figure 4.6, the z-component of the top as well as the spin frequency is shown. The two plots show that the implemented driving system works as expected as the top is kept levitating while its spin frequency remain constant in an oscillatory fashion.

In order to obtain the result it is necessary to slightly adjust the initial spin frequency in order to synchronize the top with the driving frequency and thus achieve perpetual levitation. This is similar to the experimental situation where perpetual levitation often is obtained after several attempts. The oscillation amplitude of the spin frequency is also consistent with what has been observed experimentally.

The relation between the precession frequency and the driving frequency is treated experimentally in Chapter 3 and this can now be investigated numerically. In Figure 4.7 precession frequency is shown. The specific time interval is chosen at a high time to avoid the more irregular behavior at start. The derivative changes rapidly and it is clearly not fixed around a certain value as could be expected from the experimental result. However, by inspection the mean value of the curve over the interval is close to 30 Hz which suggests that there may be some kind of periodicity. By looking directly at the angle ϕ it is possible to find the experimentally observed synchronization between the precession and driving field. This is shown in Figure 4.8 below. The precession frequency is not strictly periodic and has rather chaotic behavior at certain points but over the entire interval the number of completed revolutions matches the driving frequency. The amount of wiggles and bumps decreases for increased times but are still present at times greater than 300 seconds.

4.5 Animation

Solving the equations of motion yields the full time dependence of all coordinates which means that the both the position and orientation of the top is known at all times. However, it is hard to interpret the Euler angles and their derivatives from plotted data. An amusing but also quite informative way to present the solution is animation. This is a good reality check to see if the calculated result is qualitatively consistent with the experimental observations. Animations are not very suitable in paper format and is thus not discussed any further in this thesis. For the interested reader, a selection of animations will appear on http://www.kiko.fysik.su.se/en/thesis.html.

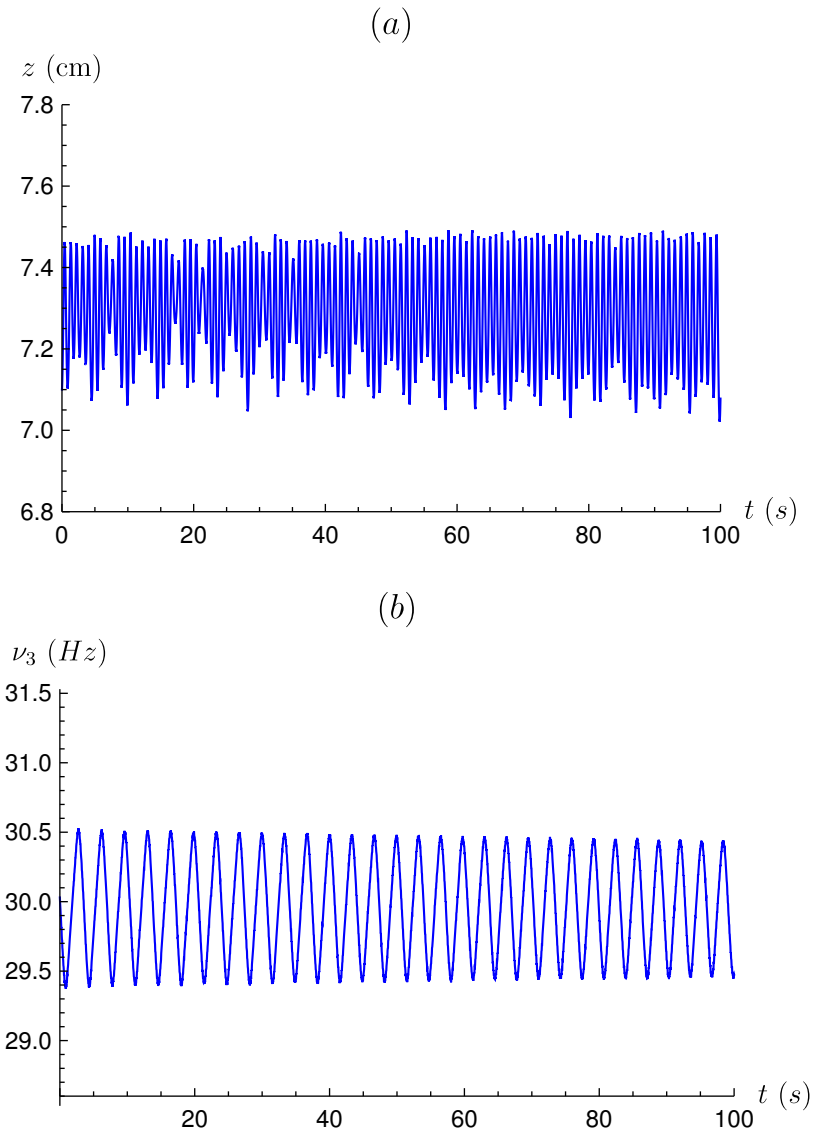

Figure 4.6: The z-component of the top as a function of time (a) and the corresponding spin frequency (b) for the first initial condition. The driving frequency used is 30 Hz.

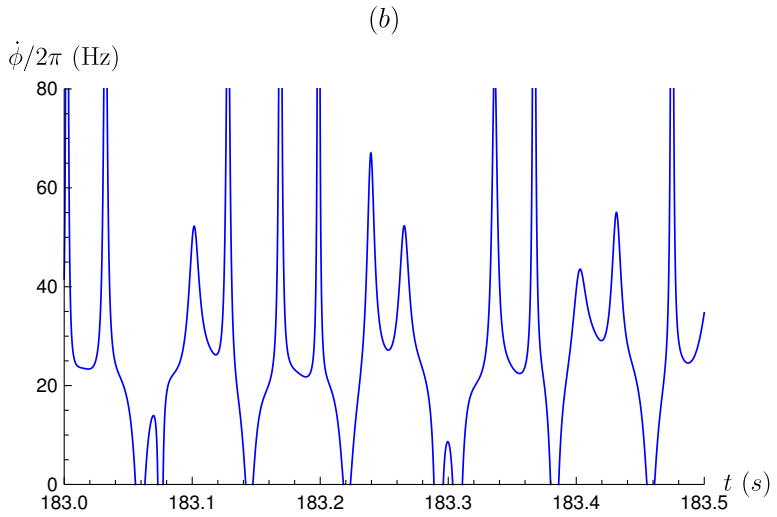

Figure 4.7: The precession frequency $\dot{\phi}/2\pi$ as a function of time.

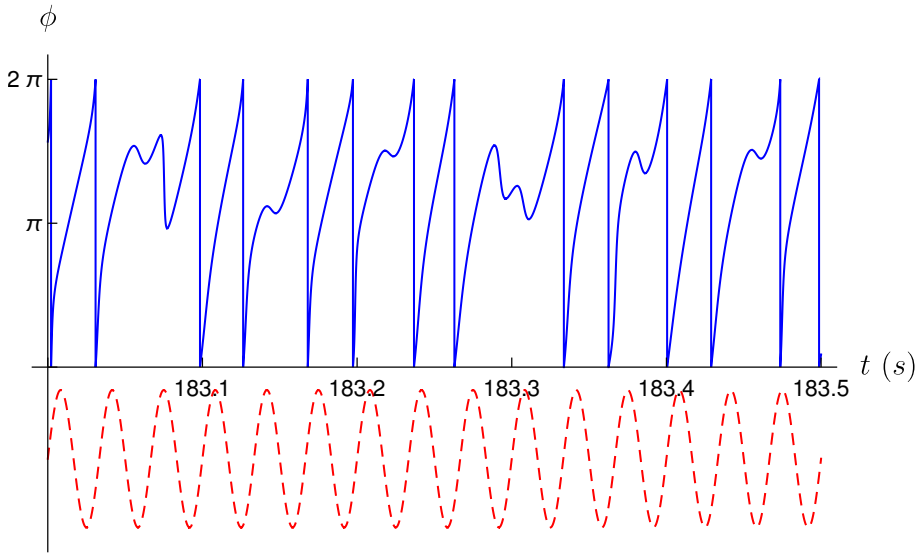

Figure 4.8: The Euler angle ϕ in blue over time. The dashed red line is the periodic part of the driving field and is included for comparison.

5. Conclusion and outlook

In this chapter the results from the previous chapters are discussed. The discussion is followed by an outlook on how the work in this thesis can be continued and expanded upon.

5.1 Conclusion

The theory, though not as extensively treated as in [1], predicts stable levitation within a height interval that is in agreement with the experimental result as well as the simulation. The theoretical lower stability limit is as previously mentioned not very accurate. By construction, it is a lower bound and is in that sense in good agreement with measurements and numerical data.

Instead of the theoretical lower limit, it is more interesting to compare the limits from the experimental observations and the simulations. The computed lower limits are very close to the experimental values, especially when air resistance is included in the simulation. It is not clear if the numerical upper stability limit would agree with a successful experimental measurement but the calculated values are above the measured lower bound. The upper stability limit is more dependent on the initial conditions than the lower limit which suggests that these results are less reliable.

The relation between the top precession and driving frequencies for a driven Levitron is also of interest. The experimental measurements show that the precession frequency depends linearly on the driving frequency. The above relation could not be reproduced convincingly in the simulation as the calculated precession frequency is highly chaotic. By instead looking at the angle ϕ over several revolutions, the mean precession frequency is found to be close to the frequency of the driving system. However, ϕ is not periodic and inherits much of the chaotic behavior from the precession and therefore the results can not be viewed as very trustworthy.

5.2 Outlook

Though the Levitron is treated quite extensively in this thesis, there are several possible ways of expanding upon the three main parts. The theory part could naturally be developed by for example introducing more advanced topics such as the geometric magnetism introduced in [1].

Measurements of the upper stability limit were not attainable using the experimental setup and the question whether the experimental stability limit agrees with the achieved numerical results is still open. This is important to make sure that the mechanism behind the upper limit is contained in the derived equations of motion. The experimental setup can be improved and expanded on to investigate more properties. The translational motion of the top for example is not examined at all and could potentially give some insightful information with the right setup. Instead of the rather crude driving system which is employed in this thesis, a more advanced system that uses feedback control would be preferable. For example, in the method used in ref. [10] the measured spin frequency is fed into the driving system. The amplitude of the produced magnetic field, instead of its frequency, is then changed to accelerate the top. It is plausible that this method makes it easier to reach high spin frequencies which means that the upper frequency limit could be measured.

When it comes to the simulation analysis, practically any possible experimental setup can be tested numerically. This include the above mentioned feedback control system or other magnetic fields. Some effect of having loose washers rotating with lower speeds could potentially be studied numerically.

6. Appendix A

6.1 The main program

ClearAll[“Global*”](*Clears preexisting variables*)

(*Declaration of functions*)

SetAttributes[{a, b, rho, I1, I2, I3, mu, m, c, miss, B0, W}, Constant]
(* Declaration and fixing of parameters *)
Rx[v_]:={{1, 0, 0}, {0, Cos[v], −Sin[v]}, {0, Sin[v], Cos[v]}};
Ry[v_]:={{Cos[v], 0, Sin[v]}, {0, 1, 0}, {−Sin[v], 0, Cos[v]}};
Rz[v_]:={{Cos[v], −Sin[v], 0}, {Sin[v], Cos[v], 0}, {0, 0, 1}};
R[phi_, theta_, psi_]:=Rz[phi].Rx[theta].Rz[psi]; (* Rotation matrix *)
phi0[z_]:=2Pirho$z$(1/(Sqrt[a^2 + z^2]) − 1/(Sqrt[b^2 + z^2]));
(* Magnetic scalar potential along the axis *)
phi1[z_]:=phi0′[z];
phi2[z_]:=phi1′[z];
phi3[z_]:=phi2′[z];
phi4[z_]:=phi3′[z];
Phi[x_, y_, z_]:=phi0[z] − 1/4phi2[z](x^2 + y^2); (* Magnetic scalar potential *)
B[x_, y_, z_] = −Grad[Phi[x, y, z], {x, y, z}]; (* Magnetic field *)
T = I1/2(theta′[t]^2 + phi′[t]^2Sin[theta[t]]^2) + I3/2(psi′[t] + phi′[t]Cos[theta[t]])^2+

$m/2(x'[t]\text{^}2 + y'[t]\text{^}2 + z'[t]\text{^}2);$

$U = -(R[\text{phi}[t], \text{theta}[t], \text{psi}[t]].\{\text{missmu}, 0, (1 - \text{miss}) * \text{mu}\}).B[x[t], y[t], z[t]] +$

$mgz[t] - \text{B0Cos}[2\text{Pi}Wt](R[\text{phi}[t], \text{theta}[t], \text{psi}[t]].\{\text{missmu}, 0, (1 - \text{miss}) * \text{mu}\})[[2]];$

$L = T - U;$

(*Euler − Lagrangeequations*)

eqs = {

$\text{Dt}[D[L, x'[t]], t] - D[L, x[t]] == 0,$

$\text{Dt}[D[L, y'[t]], t] - D[L, y[t]] == 0,$

$\text{Dt}[D[L, z'[t]], t] - D[L, z[t]] == 0,$

$\text{Dt}[D[L, \text{phi}'[t]], t] - D[L, \text{phi}[t]] == -c\ \text{Cos}[\text{theta}[t]](\text{phi}'[t]\text{Cos}[\text{theta}[t]] + \text{psi}'[t]),$

$\text{Dt}[D[L, \text{theta}'[t]], t] - D[L, \text{theta}[t]] == 0,$

$\text{Dt}[D[L, \text{psi}'[t]], t] - D[L, \text{psi}[t]] == -c(\text{phi}'[t]\text{Cos}[\text{theta}[t]] + \text{psi}'[t])$

}//Simplify;

(*Parameters*)

$a = 3$; (* Inner radius *)

$b = 5.5$; (* Outer radius *)

$\text{miss} = 0.03$; (* Dipole missalignment *)

$\text{mu} = -7140$; (* Dipole moment *)

$\text{rho} = 140$; (* Dipole density *)

$\text{I1} = 10.4$; (* Transversal moment of inertia *)

$\text{I3} = 17.31314$; (* Vertical moment of inertia *)

$m = 24.45$; (* Top mass *)

```
B0 = 0.4; (* Driving field strength *)
W = 30; (* Driving frequency *)
g = 982; (* Gravitational acceleration *)
c = 0.00318175 * I3;
(* Frictional constant *)

(* Initial conditions *)
T = 30; (* Max simulation time*)
x0 = 0.1;  (*Initialx - value*)
z0 = 7.1;  (*Initialz - value*)
xpr0 = -0.07;  (*Initialx' - value*)
zpr0 = 0.2;  (*Initialz' - value*)
theta0 = 0.01;  (*Initialtheta' - value*)
nu0 = 30.03; (* Initial spin frequency *)
psipr0 = 2Pinu0/(Cos[theta0] + 1);

(*Latex - styleplotlabels*)

<< MaTeX
zlab = MaTeX["z \\ (\\mathrm{cm})", Magnification -> 0.9];
xlab = MaTeX["x \\ (\\mathrm{cm})", Magnification -> 0.9];
ylab = MaTeX["y \\ (\\mathrm{cm})", Magnification -> 0.9];
nulab = MaTeX["\\nu_3 \\ (Hz)", Magnification -> 0.9];
tlab = MaTeX["t \\ (s)", Magnification -> 0.9];


(* Solving the ODE numerically*)
```

```
TMax = T;
r = NDSolve[{eqs, x[0] == x0, y[0] == 0.0, z[0] == z0, x'[0] == xpr0, y'[0] == 0.0,
z'[0]==zpr0, phi[0]==0.0, theta[0] == theta0, psi[0] == 0.0, phi'[0] == psipr0,
theta'[0] == 0.0, psi'[0] == psipr0, WhenEvent[{z[t] == 0, x[t]^2 + y[t]^2 ==  4},
{TMax = t, "StopIntegration"}]}, {x, y, z, phi, theta, psi}, {t, 0, T}, Method->"BDF"];


(* Top 3D Graphics *)


rmitt = 0.34;
hmitt = 3.3;
rring = 1.44;
hring = 0.33;
rplatta = 1.23;
hplatta = 0.07;
rhole = 0.34;
rlplatta = 0.98;
rlhole = 0.38;
rlmplatta = 1.02;
h0ring = 0.7;
RCM = "0.831138";
P = Cylinder[{{0, 0, 0}, {0, 0, hmitt}}, rmitt];
P2 = Cylinder[{{0, 0, h0ring}, {0, 0, h0ring + hring}}, rring];
P3 = Cylinder[{{0, 0, h0ring + hring}, {0, 0, h0ring + hring + hplatta}}, rplatta];
P4 = Cylinder[{{0, 0, h0ring + hring + hplatta}, {0, 0, h0ring + hring + 2hplatta}}, rplatta];
```

```
P5 = Cylinder[{{0, 0, h0ring + hring + 2hplatta}, {0, 0, h0ring + hring + 3hplatta}}, rlmplatta];
P6 = Cylinder[{{0, 0, h0ring + hring + 3hplatta}, {0, 0, h0ring + hring + 4hplatta}}, rplatta];
P7 = Cylinder[{{0, 0, h0ring + hring + 6.5hplatta}, {0, 0, h0ring + hring + 8hplatta}}, 0.4];
P9 = Cylinder[{{0, 0, h0ring + hring + 4hplatta}, {0, 0, h0ring + hring + 5hplatta}}, rlplatta];
P8 = Cone[{{3rlplatta/4, 0, h0ring + hring + 5hplatta},
{3rlplatta/4, 0, h0ring + hring + 6hplatta}}, rmitt/5];
S = {P, P2, P3, P4, P5, P6, P7, P8, P9};

(* Example plots *)


Plot[Evaluate[z[t]/.r], {t, 0, TMax}, AxesLabel → {tlab, zlab},
PlotRange → {{0, TMax}, {6.8, 7.8}}];
(* Top height as function of time *)
Plot[Evaluate[(phi'[t]Cos[theta[t]] + psi'[t])/.r][[1]]/(2Pi), {t, 0, TMax},
AxesLabel → {tlab, nulab}, PlotRange → {{0, TMax}, {nu0 − 1.5, nu0 + 1.5}}];
(* Spin frequency as function of time *)
ParametricPlot[{Evaluate[x[t]/.r][[1]], Evaluate[z[t]/.r][[1]]}, {t, 0, TMax},
AxesLabel → {xlab, zlab}, PlotStyle->{Blue, AbsoluteThickness[0.8]},
AxesOrigin → {−0.4, 7.0}, PlotRange → {{−0.4, 0.4}, {7.0, 7.6}}];
(*Projectiononxz − plane*)

(*Animation*)


Manipulate[F1 =
GeometricTransformation[S, RotationTransform[Evaluate[psi[t]/.r][[1]], {0, 0, 1}]];
F2 = GeometricTransformation[F1, RotationTransform[Evaluate[theta[t]/.r][[1]], {1, 0, 0}]];
F3 = GeometricTransformation[F2, RotationTransform[Evaluate[phi[t]/.r][[1]], {0, 0, 1}]];
```

```
R = GeometricTransformation[F3, TranslationTransform[{Evaluate[x[t]/.r][[1]],
Evaluate[y[t]/.r][[1]], Evaluate[z[t]/.r][[1]] - RCM}]];
Graphics3D[{EdgeForm[None], R}, PlotRange → {{-3, 3}, {-3, 3}, {0, 10}}, Axes → True,
AxesLabel → {xlab, ylab, zlab}], {{t, 0}, 0, TMax, AnimationRate → 1/10,
RefreshRate → 120}, SaveDefinitions → True, AutorunSequencing → 15];
```

List of Figures

List of Tables

Acknowledgements

I would like to thank my main supervisor Ingemar for his excellent guidance, his commitment to this thesis and especially all his time spent proofreading this text. I would also like to thank my supervisor Sven-Olof for suggesting this this very interesting project and always contributing with exciting new points and ideas. This project would not have been possible without the technical expertise of my supervisor Lars and I am grateful for all his help. The many hours we spent in the lab were very enjoyable. Finally, I would like to give my thanks to Andreas Rydh for his assistance with acquiring equipment to the experiment.

References

[1] M. V. Berry. The Levitron$^{\text{TM}}$: An adiabatic trap for spins. *Proceedings of the Royal Society Series A*, **452**:1207–1220, 1996. 2, 10, 12, 17, 41, 42

[2] M. V. Berry and A. K. Geim. Of flying frogs and levitrons. *European Journal of Physics*, **18**:307–313. 5

[3] S. Earnshaw. On the nature of the molecular forces which regulate the constitution of the luminiferous ether. *Transactions of the Cambridge Philosophical Society*, **7**:97–112, 1842. 4

[4] H. Goldstein, J. L. Safko, and C. P. Poole. *Classical mechanics*. Addison-wesley, 3 edition, 2005. 8, 9, 20

[5] M. E. Grugel. Modeling the viscous torque acting on a rotating object. *Journal of Chemical Physics*, **104**(20). 20

[6] J. D. Jackson. *Electrodynamics*. Wiley, 3 edition, 1991. 13

[7] W. Paul. Electromagnetic traps for charged and neutral particles. *Reviews of Modern Physics*, **62**(2). 5

[8] F. Scheck. *Mechanics - From Newton's laws to deterministic chaos*. Springer, 3 edition, 1991. 6, 7, 8

[9] Mike & Karen Sherlock. The hidden history of the Levitron, 1999. [http://amasci.com/maglev/lev/expose1.html; accessed 25-April-2017]. 2

[10] M. D. Simon, L. O. Heflinger, and S. L. Ridgway. Spin stabilized magnetic levitation. *American Journal of Physics*, **65**:286–292, 1997. 2, 18, 25, 35, 42

[11] E. Süli and D. F. Mayers. *An Introduction to Numerical Analysis*. Cambridge University Press, 2003. 31